1964

Heat transfer in the region of interaction of an oblique shock wave and a laminar boundary layer

William John Cook
Iowa State University

HEAT TRANSFER IN THE REGION OF INTERACTION OF AN OBLIQUE SHOCK WAVE AND A LAMINAR BOUNDARY LAYER

by

William John Cook

A Dissertation Submitted to the
Graduate Faculty in Partial Fulfillment of
The Requirements for the Degree of
DOCTOR OF PHILOSOPHY

Major Subjects: Mechanical Engineering
Theoretical and Applied Mechanics

Approved:

Signature was redacted for privacy.

In Charge of Major Work

Signature was redacted for privacy.

Heads of Major Departments

Signature was redacted for privacy.

Dean of Graduate College

Iowa State University
Of Science and Technology
Ames, Iowa

1964

TABLE OF CONTENTS

LIST OF SYMBOLS

Symbol	Units	Description
a_1	ft/sec	Sonic velocity at T_1
a_2	ft/sec	Sonic velocity in region 2
C_f		Skin-friction coefficient, τ_w/Q_2
C_p		Pressure coefficient, $(P-P_2)/Q_2$
C_{pi}		Incipient separation pressure coefficient
C_{pp}		Plateau pressure coefficient
C_{ps}		Separation pressure coefficient
C_{p4}		Pressure coefficient for the regular reflection of a shock wave
c_p	Btu/lbm °R	Constant pressure specific heat
c_v	Btu/lbm °R	Constant volume specific heat
E	volts	Voltage
E_{fo}	volts	Initial thin-film gage voltage
h_i	lbm/ft^2 sec	Heat-transfer coefficient defined by Equation 19
I	amperes	Current
i	Btu/lbm	Enthalpy
i*	Btu/lbm	Reference enthalpy
i_{aw}	Btu/lbm	Enthalpy at T_{aw}

Symbol	Units	Description
i_2	Btu/lbm	Free-stream static enthalpy
i_2°	Btu/lbm	Free-stream stagnation enthalpy
k	Btu/ft sec °R	Thermal conductivity
M_2		Free-stream Mach number - also region 2 Mach number
M_{2r}		Mach number in region 2 relative to normal shock wave
M_s		Mach number of normal shock wave, V_s/a_1
Nu		Local Nusselt number, hx/k
(Nu/Pr)*		$h_i x/\mu^*$
P	lbf/ft^2 or mm Hg abs	Pressure
P_1	lbf/ft^2 or mm Hg abs	Initial shock-tube channel pressure
P_2	lbf/ft^2 or mm Hg abs	Free-stream static pressure - also region 2 pressure
P_4	lbf/ft^2 or mm Hg abs	Free-stream static pressure downstream of a regular reflection
P_6	lbf/ft^2 or mm Hg abs	Initial shock-tube chamber pressure
Pr		Prandtl number, $c_p\mu/k$
Pr*		Prandtl number with temperature dependent properties introduced at i*
q	Btu/ft^2 sec	Local heat-transfer rate

Symbol	Units	Description
q'	Btu/ft^2 sec	Local heat-transfer rate in the shock-wave boundary-layer interaction region
q_{fp}	Btu/ft^2 sec	Local theoretical heat-transfer rate for undisturbed laminar flat plate flow
$\bar{q}'_s$	Btu/ft^2 sec	Average heat-transfer rate in a separated region
$\bar{q}_{fps}$	Btu/ft^2 sec	Average theoretical flat-plate heat-transfer rate for an attached boundary layer at the separated region location
Q_2	lbf/ft^2	Free-stream dynamic pressure, $\rho_2 V_2^2/2g_c$
R	lbf ft/lbm °R	Gas constant
R_f	Ohms	Thin-film electrical resistance
R_{fo}	Ohms	Initial thin-film gage electrical resistance
Re_o		Reynolds number based on free-stream properties and x_o
Re_i		Reynolds number based on free-stream properties and x_i
Re_g		Reynolds number based on free-stream properties and x_g
Re_2		Reynolds number based on free-stream properties and x

Symbol	Units	Description
Re^*		Reynolds number based on x with temperature-dependent properties introduced at i*
r		Recovery factor defined by Equation 17
St_i^*		Stanton number, $h_i/(\rho^* V_2)$
T	°R	Temperature
T_{aw}	°R	Adiabatic wall temperature
T_o	°R	Initial uniform temperature of semi-infinite solid
T_w	°R	Wall temperature - also initial model temperature ($T_w = T_1$ in experimental investigation)
T_1	°R	Initial temperature of test gas in shock-tube channel
T_2	°R	Free-stream static temperature - also temperature in region 2
T_2°	°R	Free-stream stagnation temperature
t	seconds, or microseconds	Time
t_f	microseconds	Flow time, measured from the arrival of the normal shock at the heat-transfer gages
V_s	ft/sec	Velocity of normal shock wave in shock-tube flow
V_2	ft/sec	Free-stream velocity

Symbol	Units	Description
V_{2r}	ft/sec	Velocity in region 2 relative to the normal shock wave
x	inches or feet	General distance from the leading edge of the flat plate
x_i	inches or feet	The value of x where the incident shock wave intersects the flat-plate surface - see Figures 1A and 2A
Δx_i	inches	Theoretical variation in x_i
x_g	inches or feet	x location of thin-film heat-transfer gages
x_o	inches or feet	The value of x where boundary-layer thickening due to the shock-wave boundary-layer interaction begins, see Figure 2A
x_r	inches or feet	The value of x at which reattachment occurs
x_s	inches or feet	The value of x at which separation occurs
X	inches or feet	Distance from the diaphragm in the shock tube
α	$(°R)^{-1}$	Temperature coefficient of resistance for thin-film gage
α_1		$(\gamma_1 + 1)/(\gamma_1 - 1)$
β		$(M_2^2 - 1)^{1/2}$
β_1		$(\gamma_1 - 1)/2\gamma_1$
β_6		$(\gamma_6 - 1)/2\gamma_6$

Symbol	Units	Description
Γ	$Btu/ft^2\ {}^\circ R(sec)^{1/2}$	$(k\rho c_p)^{1/2}$ of thin-film gage backing material
δ	inches or feet	Boundary layer thickness
γ		Specific heat ratio c_p/c_v
γ_1		c_p/c_v for the test gas
γ_6		c_p/c_v for the shock-tube driver gas
ρ	lbm/ft^3	Density
μ	lbm/ft sec	Viscosity
μ^*	lbm/ft sec	Viscosity at T*
θ		Flow-deflection angle, Figure 1A
$\propto$		Proportional sign
τ_w	lbf/ft^2	Shearing stress at the wall
τ		Variable of integration in Equation 30

INTRODUCTION

An important consideration in the design of many present day supersonic flight vehicles is the aerodynamic heating rate. Minimum heat-transfer rates are usually associated with laminar boundary layers, and since supersonic vehicles undergo flight conditions where the boundary layer flow is laminar over part or all of the vehicle surface, the study of phenomena affecting heat transfer through the supersonic laminar boundary layer is of practical importance.

One of the phenomena which has a disturbing effect on the supersonic laminar boundary layer is the incidence of a shock wave on the surface where the boundary layer is present. The resulting interaction between the shock wave and the boundary layer has been the subject of a number of experimental and theoretical investigations, most of which have been devoted to the study of the flow pattern and the skin-friction and pressure distribution in interactions occuring on insulated surfaces. Apparently no comprehensive study of heat transfer in the region of interaction has been made. Thus the present investigation was initiated to study primarily by experimental means the heat-transfer rates in the region of interaction of a shock wave and a laminar boundary layer.

Prior to outlining in detail the scope of the present investigation, previous work related to the shock-wave boundary-layer interaction will be reviewed in the following

section. The order of presentation is somewhat chronological with related experimental studies being discussed first since several of the theoretical studies reviewed were primarily an outgrowth of the knowledge gained from the experimental studies. Considerable attention is given to shock-wave boundary-layer interactions occuring on insulated surfaces since the results of these studies provide the groundwork for the investigation of heat-transfer rates in the interaction region.

REVIEW OF RELATED WORK

Regular Reflection of a Shock Wave

Figure 1A illustrates the reflection in inviscid two-dimensional flow of an oblique shock wave incident on a flat surface. The incident shock wave is considered to be generated by a wedge placed in the supersonic stream. The flow initially parallel to the flat-plate surface in region 2 is turned toward the plate surface as it passes through the incident shock wave. The incident shock wave reflects as a second oblique shock wave which turns the flow again parallel to the plate surface in region 4. Reflections of this nature are termed regular reflections.

Figure 1B shows the pressure distribution on the plate surface that would exist for the regular reflection illustrated in Figure 1A. The step change in pressure that results from the regular reflection can be calculated from well-known theoretical relations. The pressure ratio P_4/P_2 for regular reflections is shown in Figure 1C as a function of the wedge flow-deflection angle θ in Figure 1A for a Mach number in region 2 of 1.5. The pressure coefficient for the regular reflection is

$$C_{p4} = \frac{P_4 - P_2}{Q_2} = \frac{2}{\gamma M_2^2}\left(\frac{P_4}{P_2} - 1\right).$$

The regular reflection is of interest here since the pressure

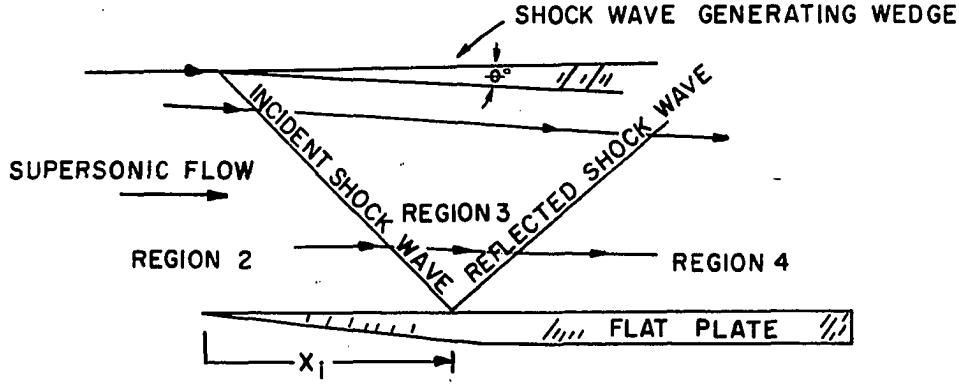

Figure 1A. Regular reflection of a shock wave

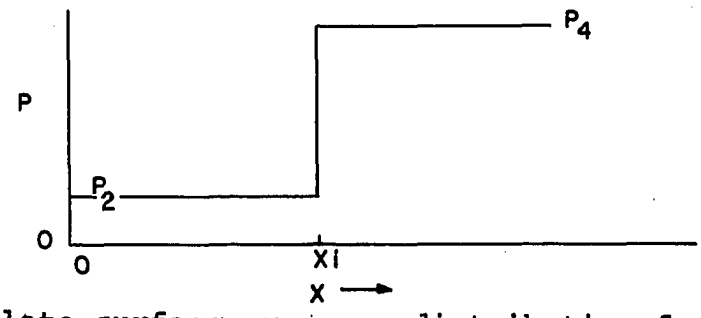

Figure 1B. Plate-surface pressure distribution for a regular reflection

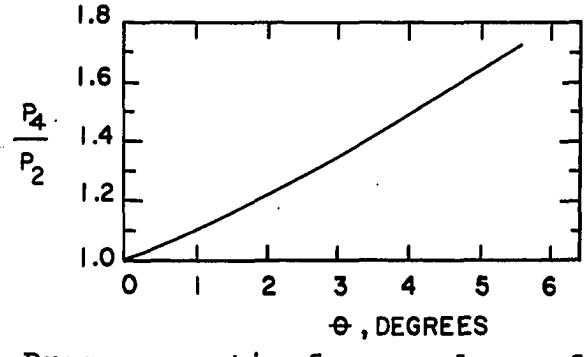

Figure 1C. Pressure ratio for regular reflections for a region 2 Mach number of 1.5

rise accompanying it has a direct bearing on the shock-wave boundary-layer interaction.

Shock-Wave Boundary-Layer Interactions

Attention was drawn to the interaction of a shock wave and a boundary-layer by Ferri (1) in 1939. Ferri observed boundary-layer separation in a supersonic wind tunnel near the trailing edge of an airfoil where a recompression shock formed. In 1947, Fage and Sargent (2) published a study of the interaction of normal and oblique shock waves with a turbulent boundary-layer on the flat wall of a supersonic wind tunnel. Later Ackert, et al., (3) studied shock-wave boundary-layer interactions on curved surfaces in transonic flow, as did Liepmann (4) in a similar study at about the same time. An important contribution of these investigations was the observation that the nature of the interaction depended to a great extent on whether the boundary layer was laminar or turbulent.

Experimental studies of adiabatic pure-laminar interactions

During the 1950's several experimental studies of shock-wave boundary-layer interactions were reported. The results of these studies provide an insight into the nature of the interaction. Particularly noteworthy are the investigations of Liepmann and Roshko (5), Barry et al. (6), Gadd et al. (7), Chapman et al. (8), and Hakkinen et al. (9). Each of these studies was carried out in a wind tunnel using flat-plate and wedge models similar to those in Figure 1A under essentially

adiabatic interaction conditions. The interaction flow patterns were recorded using Schlieren photographic techniques. For the adiabatic interaction it was found that the principal factors affecting the interaction were the Mach and Reynolds numbers and the incident shock strength. Other general and specific results of these investigations provide the basis for the following discussion.

Figure 2A shows schematically the experimentally observed interaction between an oblique shock wave and a laminar boundary-layer on an insulated surface. This illustration is for a case where the adverse pressure gradient created by the incident shock wave is strong enough to cause boundary layer separation, but not strong enough to cause transition from laminar to turbulent flow in the boundary layer. Chapman et al. (8) identify separated flows in which the boundary layer remains laminar on reattachment as pure-laminar separated flows. The interaction depicted in Figure 2A is therefore identified herein as a pure-laminar interaction.

Typically, in a pure-laminar interaction which involves separation, the boundary layer thickens and then separates at x_s from the wall upstream of the incident shock and reattaches at x_r some distance downstream while a region of low-velocity reversed flow (sometimes termed the "dead-air" region) is generated between the wall and the separated boundary layer. Accompanying the separation is the formation of compression and expansion regions extending into the free stream and the

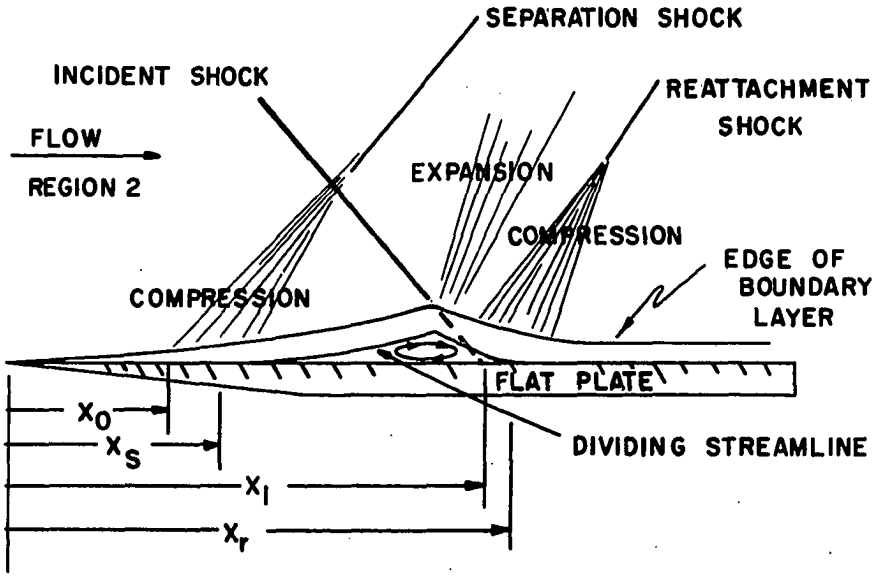

Figure 2A. Pure laminar shock-wave boundary-layer interaction (interaction exaggerated)

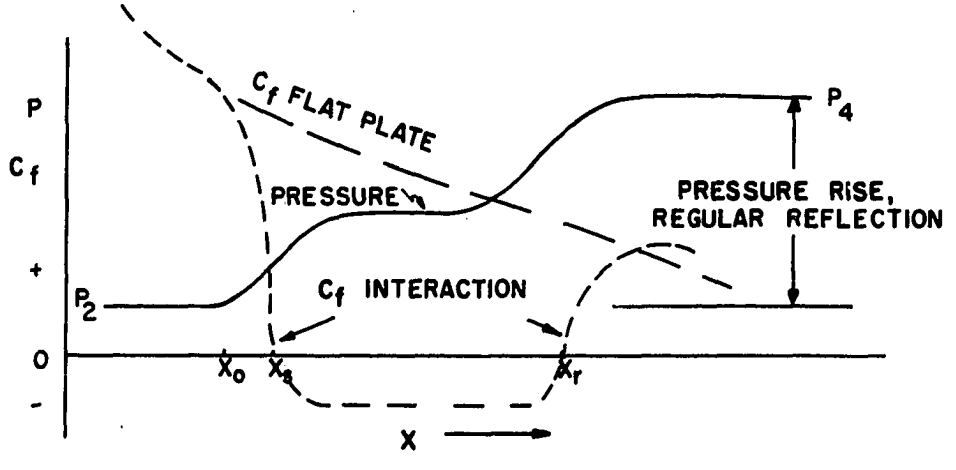

Figure 2B. Pressure and wall-friction distribution for a pure-laminar interaction

formation of shock waves in the external flow. This results in a reflected shock-wave pattern considerably different than that of the regular reflection illustrated in Figure 1A.

Not all incident shock waves cause boundary layer separation nor does the boundary layer in all separated-flow interactions remain laminar. For relatively weak incident shock waves, boundary layer separation is not observed. For sufficiently large values of shock strength, boundary layer separation occurs, and if the Reynolds number is sufficiently low, the boundary layer remains laminar on reattachment. Interactions involving transition from laminar to turbulent flow are discussed in the following section.

Referring again to Figure 1C, the pressure ratio P_4/P_2 for the regular reflection is seen to increase with the angle θ. Local pressure measurements in references 6, 7, and 9, indicate that a feature common to all shock-wave boundary-layer interactions is that the ultimate static wall pressure rise is nearly the same as that for the regular reflection, although the pressure distribution in the region of interaction differs considerably from the step in pressure associated with the regular reflection. Figure 2B shows a typical wall pressure distribution curve observed for the pure-laminar interaction illustrated in Figure 2A.

The subsonic portion of the boundary layer next to the wall plays an important role in the development of the interaction pattern. Pressure disturbances which cannot propagate upstream

in supersonic flow do propagate upstream in subsonic flow. In addition, the subsonic layer cannot sustain the large pressure gradient that occurs as a result of the impingement of the incident shock wave. As a result, the region in which pressure rises extends upstream and downstream of the point of shock-wave incidence as shown in Figure 2B. The thickening of the boundary layer that results upstream deflects the external flow from its original free-stream direction and generates a band of compression waves as shown in Figure 2A. Equilibrium between boundary-layer thickening and the compression process in the external stream governs the shape of the pressure distribution in the region of the boundary layer separation point. As the rate of change of thickening of the viscous region decreases, the positive pressure gradient decreases resulting in a region of constant pressure. This region is identified as the "pressure plateau" by Hakkinen et al. (9).

Since the subsonic portion of the flow cannot support a sudden pressure rise, the incident shock must be reflected from the boundary layer as an expansion fan which cancels the pressure rise across the incident shock wave. Because of this expansion region the flow external to the viscous layer is turned toward the wall accounting for the fact that the thickness of the viscous layer is observed to begin decreasing as shown in Figure 2A, that is, the viscous region is compressed by the external flow.

The remainder of the pressure rise is associated with

compression waves which coalesce to the reflected shock wave which forms outside the viscous region. Chapman et al. (8) state that the pattern of compression and expansion waves shown in Figure 2A is an identifying feature of all pure-laminar shock-wave boundary-layer interactions. Accompanying the downstream pressure increase is a deceleration of the flow in the viscous layer on reattachment. The flow in the lower velocity regions near the wall which does not possess sufficient kinetic energy to penetrate the region of increasing pressure is turned back upstream, and, as a result, a region of reversed flow is generated in which mass is entrained. The remainder of the flow passes on downstream to form the downstream boundary layer. The streamline which separates the entrained mass and the flow which passes downstream is denoted as the dividing streamline.

Hakkinen, et al. (9) measured velocity profiles in the region of interaction for the insulated pure-laminar interaction and found that the velocity profiles in the region above the reversed flow region were similar to those in the undisturbed constant pressure profile. Figure 2B shows the typical skin-friction coefficient profile for a pure-laminar interaction. Also shown is the corresponding skin-friction coefficient for undisturbed flat-plate flow. The profile for positive C_f values is verified by measurements in reference 9. The values of C_f in the reversed flow region are considered in the literature to be negative.

Experimental data (6, 7, 9) related to the extent of the interaction region indicate an effect of three parameters, the incident shock strength, the Mach number, and the Reynolds number, on the interaction length of the pure-laminar interaction. For fixed Mach and Reynolds numbers, increased shock strength results in increased interaction length. Decreasing Reynolds number at fixed Mach number and shock strength also results in increased interaction length. Increasing Mach number for given Reynolds numbers and shock strength results in a decrease in interaction length.

Experimental results presented by Barry et al. (6) indicate that for adiabatic interactions the ratio $(x_i - x_o)/x_i$ in Figure 2A is a function only of Reynolds number and the shock strength at a given Mach number. The experimental work of Gadd et al. (7) shows that an equation of the form

$$\left(\frac{x_i - x_o}{x_o}\right)(Re_o)^{-1/4} = f(M_2, C_{p4}) \qquad \text{Eqn. 1.}$$

roughly described the upstream extent of pure laminar interaction. Re_o is the Reynolds number based on free stream fluid properties and x_o. Equation 1 is the result of an unpublished theoretical analysis performed by Gadd.

Experimental studies of adiabatic transitional interactions

Through the analysis of a large number of experimentally observed adiabatic separated flows associated with several

geometries, Chapman et al. (8) have observed that an important variable in flows involving boundary-layer separation is the location of boundary layer transition relative to the separation and reattachment points. If transition from laminar to turbulent flow takes place between separation and reattachment, reference 8 classes the separated flow as "transitional".

Two features common to all pure-laminar interactions are relatively small increases in pressure and gradual changes in pressure in the interaction region. However, both of these features are not in general present in transitional interactions. Experimental results of Gadd et al. (7) and Chapman et al. (8) show that although the ultimate pressure rise in the interaction remains nearly the same as that for a regular reflection, there is, on transition a tendency toward a new pressure profile in the interaction region characterized by larger pressure gradients and a decrease in the interaction length. Severe pressure gradients were clearly observed to occur at the location where transition took place if transition occured near reattachment. It was also observed (8) that if transition took place upstream of reattachment, the reflected reattachment shock wave formed partially within the boundary layer, and only as transition moved upstream of separation did the separation shock wave form partially within the boundary layer. In the pure-laminar interaction each of these shock waves were formed by compression fans extending into the flow external to the boundary layer. Therefore, when transition

takes place just upstream of reattachment it would be expected that the separation shock wave would form as in the pure-laminar interaction.

As would be expected, increasing the Reynolds number beyond a certain value in a laminar interaction involving separation occurring at a fixed Mach number and shock strength causes a shift from the pure-laminar interaction to the transitional interaction. Shock strengths beyond a certain value also cause transition. The experimental data in reference 8 for several flow-separation-inducing geometries clearly show a trend to more stable interactions with increasing Mach number. The same Mach number stabilizing effect was observed in laminar separated flow studies by Bogdanoff and Vas (10). This indicates that pure-laminar shock-wave boundary-layer interactions might well be expected under flight conditions at high Mach numbers.

When the boundary layer is completely turbulent (i.e., transition occurs well upstream of the shock impingement point) the shock-wave boundary-layer interaction differs markedly from the interaction involving the laminar boundary layer. The major difference results from a pronounced reluctance of the turbulent boundary layer to separate.

Experimental investigations related to heat transfer in shock-wave boundary-layer interactions

Apparently the only published experimental investigation

of heat transfer in the region of interaction of a shock wave and a boundary layer is that of Sayano (11). Heat transfer in the region of interaction of an oblique shock wave and a turbulent boundary layer was studied in a supersonic wind tunnel on internally cooled flat-plate models. It was found that heat-transfer rates throughout the interaction region were larger than the undisturbed turbulent flat-plate values with peak heat-transfer rates occurring downstream of shock impingement at local rates of 2 to 9 times the values for the undisturbed turbulent boundary layer. In view of the marked difference between laminar and turbulent shock-wave boundary-layer interactions, Sayano's results are not pertinent to this investigation.

Several experimental heat-transfer investigations are indirectly related to heat transfer in shock-wave boundary-layer interactions. As will be discussed in the following sections, certain similarities exist among all supersonic separated flows in a given flow regime. Therefore, heat-transfer studies of separated flows induced by means other than an impinging shock wave become of interest.

Larson (12) found that the average heat transfer in a separated region for pure-laminar supersonic separation was 56 per cent of that for an equivalent attached boundary layer with results essentially independent of Mach and Reynolds number. Larson's study was carried out in a wind tunnel using electrically heated axially symmetric and two-dimensional

models with surface depressions (cavities) located somewhat back from the leading edge to create a region of separated flow. Flows at a free-stream Mach numbers of approximately three and four were studied and the Reynolds number based on the length from the leading edge to the termination of the cavity was varied from 1×10^5 to 40×10^5. Maximum local heat-transfer rates measured in the separated region for the axially symmetric models occured in the reattachment zone below the dividing streamline.

Experimental data from a study to determine the relation between wall cooling, transition Reynolds number, and Mach number for separated flow are also presented in reference (12). Extreme cooling of ogive-cylinder models caused a decrease in the transition Reynolds number at a given Mach number (i.e., a destabilizing effect resulted from extreme cooling). This destabilizing effect was the inverse of the stabilizing effect observed for moderate cooling and heating of attached laminar boundary layers by Jack et al. (13).

Bogdanoff and Vas (10) measured heat-transfer rates in laminar separated flow at high Mach numbers for several separation-inducing geometries, two of which are pertinent to this investigation; a flat-plate model with a forward-facing ramp on the surface back from the leading edge (compression corner model) and a cone model with a circumferential cavity located downstream of the nose. The experimental work was carried out in a hypersonic helium tunnel with the models

moderately cooled. At a Mach number of 11.7 the average heat-transfer rate in the cavity region of the cone model was approximately 50% of the average that would be expected at the same location on a solid cone, while heat-transfer rates in the region of reattachment were higher than local rates observed on solid cones at the same location. The 50% factor for the separated region was independent of Reynolds number. On the plate-ramp models, the separated boundary layer bridged the junction of the flat plate and the ramp. At a Mach number of 11.7 and Reynolds number of 2×10^6 local heat-transfer rates in the separated region varied from the flat-plate rate at the start to 50% of local flat-plate rate just ahead of the plate-ramp junction. Reattachment heat-transfer rates were approximately 1.6 times local flat-plate rates. This increased heating rate extended somewhat downstream even though the boundary layer remained laminar. Unexplained scatter of heat-transfer rates occured in the region downstream of reattachment. The average heat-transfer rates for the separated region were approximately the same as would be expected in the region for flat-plate flow.

In a recent publication, Miller et al. (14) reported the results of laminar separated-flow heat-transfer studies on compression corner models simulating the boundary-layer separation that occurs when control surfaces are deflected on supersonic aircraft. For Mach numbers ranging from 8 to 22 and Reynolds numbers from 0.5×10^5 to 12×10^5, the observed

average heat-transfer rates in the separated regions on the models were between 60 and 80 per cent of the average rates for equivalent flat-plate flow.

In a shock-tube study of laminar separated flows behind a backward facing step Hall (15) observed a reduction of heat transfer below that for equivalent flat-plate flow. Rom and Seginer (16) performed a shock-tube study of laminar separated flows using a model similar to that used by Hall. Shock Mach numbers ranged from 4 to 10. The emphasis in this study (16) was on heat transfer in a region which included the laminar reattachment zone and a zone a short distance downstream of reattachment.

Heat transfer in this region was found to be strongly dependent on Reynolds number based on flat-plate length ahead of the step. At a Reynolds number of 2×10^5 local heat-transfer rates seven times those for undisturbed flat-plate flow occurred shortly after reattachment. The increased heating rate decreased with increasing downstream distance and leveled off at a value 3.5 times local flat-plate rates. Heat-transfer rates at a Reynolds number of 4×10^4 were as high as 2.5 times local rates in the reattachment zone and 2 times flat-plate rates a short distance downstream of reattachment. At Reynolds numbers as low as 2×10^3 heat-transfer rates ranged from less than flat-plate rates in the reattachment zone to values slightly above flat-plate rates downstream of reattachment. It is interesting to note that these increased

heating rates occurred even though the boundary layer remained laminar throughout the region investigated.

Theoretical Investigations of Shock-Wave Boundary-Layer Interactions

In recent years several theories have been developed to describe mathematically the two-dimensional shock-wave boundary-layer interaction. A large portion of the theoretical studies has dealt with the pure-laminar adiabatic interaction with emphasis on predicting the wall pressure distribution and skin-friction coefficients in the interaction region. Very little work has been done to predict the heat-transfer rates in the region of interaction, but the closely related inverse problem, the effect of heat transfer on separated flows has received attention (17, 18, 19, 20).

Early attempts at solution of the shock-wave boundary-layer interaction problem neglected coupling between the viscous region and the external flow, and as a result were in general unsuccessful. The more recent theories involve the use of the momentum integral and are developed using two different approaches. One approach is the mixing theory of Crocco and Lees (21) in which transport of momentum from the outer stream to the viscous region is considered to be a fundamental process. The other method is the Pohlhausen method (22) in which velocity profiles are assumed for the interaction region. In most cases the theories developed using these

approaches involve complicated numerical iteration procedures that are difficult to apply to practical problems.

In some cases the results are obtained for segments of the interaction region and matching of theories is required for an overall analysis of the interaction region (23). Lees and Reeves state in a very recent paper (23) that none of the attempts using these two approaches has yielded a satisfactory unified theoretical analysis, and that the results are particularly unsatisfactory for flows involving heat transfer. In this paper the authors present a theoretical analysis without any empirical features that encompasses the complete pure-laminar interaction region. The theoretical results for adiabatic interactions agree well with experimental data at moderate supersonic speeds. Application of the theory to shock-wave boundary-layer interactions involving heat transfer is presently under consideration by the authors (23).

Although many of the attempts to theoretically analyze shock-wave boundary-layer interactions fail to yield results which are applicable to the whole region of interaction, some have given satisfactory practical results for certain sections of the interaction region. Several theoretical studies pertinent to this investigation are reviewed in the following paragraphs.

Heat transfer in separated regions

An important contribution to the study of heat transfer

in separated regions was made by Chapman (24). Chapman theoretically analyzed laminar separated flows similar to those which would occur over a cavity located just behind the leading edge of a flat plate, i.e., leading edge flow separation. The following assumptions were involved:

(1) the thickness of the boundary layer at separation is zero or small compared to the cavity depth,

(2) the reattachment zone length is small compared to the length of the separated boundary layer,

(3) constant pressure exists along the separated layer,

(4) the wall is isothermal.

Chapman applied the law of conservation of energy to the region in which separation occurred and the average heat transfer to the wall was calculated. The predicted value of the average wall heat-transfer rate for air was 56 per cent of the average heat-transfer rate through an attached laminar boundary layer extending over the separation length. This result was independent of Mach and Reynolds numbers and the ratio of wall to free-stream temperature.

Larson's previously mentioned experimental investigation of separated-flow heat transfer (12) was specifically designed to verify Chapman's theory applied to separated flows in air over cavities located back from the leading edge of models where the separation boundary-layer thickness was not zero. It should be noted that application of Chapman's theory to other than leading edge separated flows requires that the

boundary layer thickness be small compared to the depth of the cavity, and suggests that the 0.56 factor be applied to the heat transfer through that portion of the attached boundary layer (generated from the leading edge under similar flow conditions) which extends over the separated region. On this basis Larson obtained very good agreement with Chapman's theory. The cavity-type separated-flow heat-transfer studies by Bogdanoff and Vas (10) also showed good agreement with Chapman's theory applied in the above-described manner.

The experimental studies of Miller (14) and Bogdanoff and Vas of heat transfer in separated regions initiated by compression-corner models gave results somewhat higher than those predicted by Chapman's theory as applied in Larson's work. There is good reason to believe that the geometry difference accounts for this. Bogdanoff and Vas suggest that for cavity-type separated flows, the flow in the separated region is dictated by the separation phenomena itself with little influence from the flow external to the separated region, while separated flows on surfaces are influenced to a much greater extent by the external flow. Thus it appears that Chapman's separate-flow heat-transfer theory is not directly applicable to separated flows occurring in shock-wave boundary-layer interactions.

Heat transfer in the reattachment zone below the dividing streamline in cavity-type laminar separated flow was theoretically studied by Chung and Viegas (25). The analysis was made

for normal reattachment and was based on Chapman's work (24). The resulting theory applied to the conditions of separated flow in Larson's investigation (12) yielded heat-transfer rates within 10 per cent of Larson's measurements. The reattachment angle in Larson's study was 45 per cent. Apparently there has been no theoretical study of heat transfer through the downstream laminar boundary layer formed by the flow above the dividing streamline. Undoubtedly the complex nature of the problem has hindered theoretical progress in this area as it has in other regions of the interaction zone.

Pressure distribution in the interaction region

Efforts to predict upstream pressure distribution and the pressure rise across the incident-reflected shock system sufficient to cause separation have met with reasonable success for the pure-laminar adiabatic interaction. Analysis is based on the concept of the "free interaction" set forth by Chapman et al. (8) and Gadd et al. (7) for separated flows. In these two extensive studies of separated flows induced on models of varying geometry (forward-facing step, compression corner, and incident-shock models), it was found for supersonic separated flows that the pressure rise to separation and the plateau pressure rise (see Figure 2B) for laminar separated flows were independent of model geometry, i.e. independent of the agency inducing separation. Separated flows free from direct influences of downstream geometry (but not free from indirect

influences) are termed "free interactions". Thus a free interaction exists upstream of the incident shock wave in the pure-laminar shock-wave boundary-layer interaction involving flow separation.

Chapman et al. (8) using a linearized analysis for the external flow and the momentum equation near the wall developed the following relation for the pressure coefficient in a free interaction.

$$C_p = \frac{P - P_2}{Q_2} \sim \sqrt{\frac{C_{fo}}{\beta}} \qquad \text{Eqn. 2.}$$

where

$$\beta = \sqrt{M_2^2 - 1} \qquad \text{Eqn. 3.}$$

Here the subscript 2 has been used to designate free-stream conditions and P is the pressure at any point in the free interaction zone. C_{fo} is the skin-friction coefficient at the start of the free interaction and would be evaluated at x_o in Figure 2A for the free interaction induced by an incident shock wave.

Hakkinen et al. (9) using momentum considerations and the experimental observation that in pure-laminar separations the boundary layer is lifted nearly undisturbed from the wall, obtained the following equations for the free-interaction pressure coefficients which are of the same form as Equation 2.

$$C_{ps} = \frac{P_s - P_2}{Q_2} = \sqrt{\frac{2C_{fo}}{\beta}} \qquad \text{Eqn. 4.}$$

$$C_{pp} = \frac{P_p - P_2}{Q_2} = 1.65\ C_{ps} \qquad \text{Eqn. 5.}$$

$$C_{pi} = 2\ C_{ps} \qquad \text{Eqn. 6.}$$

where

$$C_{fo} = \sqrt{C}\left(\frac{.644}{Re_o^{1/2}}\right) \qquad \text{Eqn. 7.}$$

and C is the Chapman - Rubesin coefficient accounting for variation in viscosity with temperature defined by

$$\frac{\mu}{\mu_2} = C\,\frac{T}{T_2} \qquad \text{Eqn. 8.}$$

Re_o is the Reynolds number based on x_o and free stream properties. Equations 4 and 5 respectively represent the pressure rise to separation and to the plateau for the pressure profile shown in Figure 2B. Equation 6 predicts the pressure rise across the incident-reflected shock system just large enough to cause separation. This equation for incipient separation resulted from the plausible reasoning that as separation starts to occur (and before the pressure plateau has developed), the

pressure distribution is symmetric about the point where the incident shock intersects the boundary layer. Each of the pressure coefficient equations showed acceptable agreement with experimental data in reference (9) for adiabatic interactions.

Hakkinen also correlated the data of Chapman, et al. (8) for laminar separated flows on models of varying geometry and found reasonable agreement with the constants of equations 4 and 5. The data in reference 8 shows that the free-interaction pressure coefficients hold for adiabatic transitional separated flows as long as transition occurs near reattachment, i.e. as long as the boundary layer in the upstream portion of the separated flow region remains laminar.

Erdos and Pallone (26) starting with an analysis similar to that used in determining the relation in Equation 2 evaluated C_{ps} and C_{pp} for the free interaction. The following equations are given in reference 26 for C_{ps} and C_{pp} for flow at low supersonic Mach numbers:

$$C_{ps} = 0.81\ Re_o^{-1/4} \sqrt{\frac{2\ C_{fo}\ Re_o^{1/2}}{\beta}} \qquad \text{Eqn. 9.}$$

$$C_{pp} = 1.81\ C_{ps} \qquad \text{Eqn. 10.}$$

where the quantity under the square-root sign is evaluated from skin-friction coefficient curves given by Van Driest (27) for flat-plate flows involving heat transfer. The constants

0.81 and 1.81 in the above equations were evaluated by Erdos and Pallone from a single set of pressure measurements presented in reference 8 for a free interaction in laminar adiabatic flow. Equations 9 and 10 showed acceptable agreement with other pressure measurements of reference 8 for low-Mach-number adiabatic free interactions. It should be noted that equations 4 and 5 and 9 and 10 are similar in form, but that the constants in corresponding equations differ. Apparently there is no experimental data to verify these equations for free interactions involving heat transfer. Plots of Equations 9 and 10 in reference 26 indicate that for free interactions involving heat transfer, C_{ps} and C_{pp} differ only slightly from those for adiabatic free interactions. Ratios of wall to free-stream temperature between 0.25 and 4.0 were considered.

Little direct information was found in the literature concerning the largest pressure rise that a laminar separated boundary layer can support in a shock-wave boundary-layer interaction without the occurrence of transition. Chapman et al. (8) observed experimentally that relations of the form of Equations 4 and 5 held well for separated flows induced by various model geometries if the pressure rise above the plateau pressure did not exceed two or three times the pressure rise to the plateau pressure. This observation implies that for adiabatic shock-wave boundary-layer interactions the pressure coefficient for incipient transition

$$C_{pt} = \frac{(P_4 - P_2)_t}{Q_2} \qquad \text{Eqn. 11.}$$

is less than three or four times the plateau pressure coefficient.

Gadd et al. (20) in comments summarizing several theories of the effect of heat transfer on separation indicates that heat transfer to a wall should make the laminar boundary layer more difficult to separate while a heated wall would be expected to have the opposite effect. The experiments discussed in reference 20 verify the latter effect.

Length of the separated region

Hakkinen et al. (9) applied the momentum-integral equation to the plateau region of the pure-laminar shock-wave boundary-layer interaction and determined the form of the equation for the length of the pressure plateau. They also fitted the equation to experimentally determined plateau lengths on flat-plate models obtained at a Mach number of two and Reynolds numbers between 1×10^5 and 6×10^5 for adiabatic pure-laminar interactions. The following equation resulted:

$$\frac{L}{x_L}\left(1-\frac{L}{x_L}\right)^{-1/8} = \frac{2.53}{\beta^{1/4}}\left[1 + \frac{\gamma-1}{2} r M_2^2\right](C_{fx_L})^{1/4}\,\Delta C_{pd} + 0.097 \qquad \text{Eqn. 12.}$$

where L is the plateau length and x_L is the length from the

leading edge of the flat plate to the termination of the pressure plateau. The constants 2.53 and 0.097 were determined from a fit to the experimental data. Hakkinen et al. consider L in Equation 12 to be the approximate length of separation. In view of the experimentally determined dependence of separation length on Mach and Reynolds number it is doubtful that Equation 12 is applicable to Mach and Reynolds numbers other than those for which the constants in the equation were determined. However, the study does theoretically relate the length of separation to the Mach number, Reynolds number (through C_{fx_L}), and to the driving pressure defined by

$$\Delta C_{pd} = C_{p4} - C_{pi} \qquad \text{Eqn. 13.}$$

$$= C_{p4} - 1.21\, C_{pp} \qquad \text{Eqn. 14.}$$

where substitution of Equations 5 and 6 into Equation 13 yields Equation 14.

Heat Transfer through a Laminar Boundary Layer on a Flat Plate in High Speed Flow

Heat transfer through a laminar boundary layer on a flat plate in continuum flow has been extensively investigated and results have reached a high degree of refinement. Flat plate conditions are defined as those in which a plane surface is exposed to a flow field of uniform properties and free-stream

velocity. It is assumed that there is no pressure gradient through the boundary layer that develops on the surface. In addition it will be assumed for this discussion that the temperature of the flat-plate surface (referred to as the wall) is uniform and constant.

The boundary layer conditions encountered in compressible laminar flow are somewhat different than those encountered in incompressible laminar flow (27, 28, 29, 30). Due to the high free-stream velocity and the zero wall velocity requirement in continuum flow, large viscous stresses are present in the boundary layer which do work on the fluid and as a result of the dissipation of this energy appreciable increases in temperature can result within the boundary layer. Figure 3A shows temperature and velocity profiles for high-velocity gas flow over an insulated surface. Due to viscous dissipation the fluid temperature at the wall is higher than the free stream temperature T_2. Velocity profiles have been found to be qualitatively similar to those for low speed flow.

Heat transfer to the fluid at the wall is governed in laminar flow by conduction in the fluid. The heat transfer rate is:

$$q = -k\frac{\partial T}{\partial y}\bigg|_{y=0} \qquad \text{Eqn. 16.}$$

The wall temperature corresponding to the case of zero wall heat transfer is designated in Figure 3A as T_{aw}, the

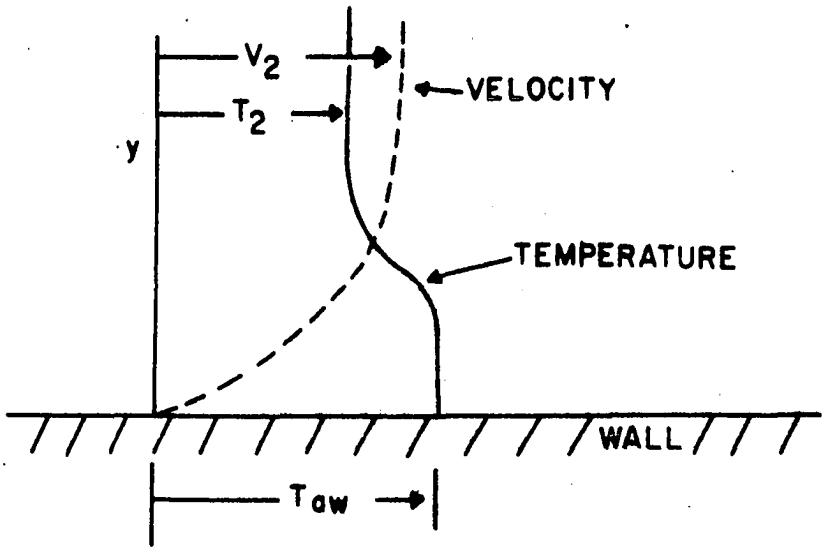

Figure 3A. Velocity and temperature distribution in high-speed flow over an insulated wall

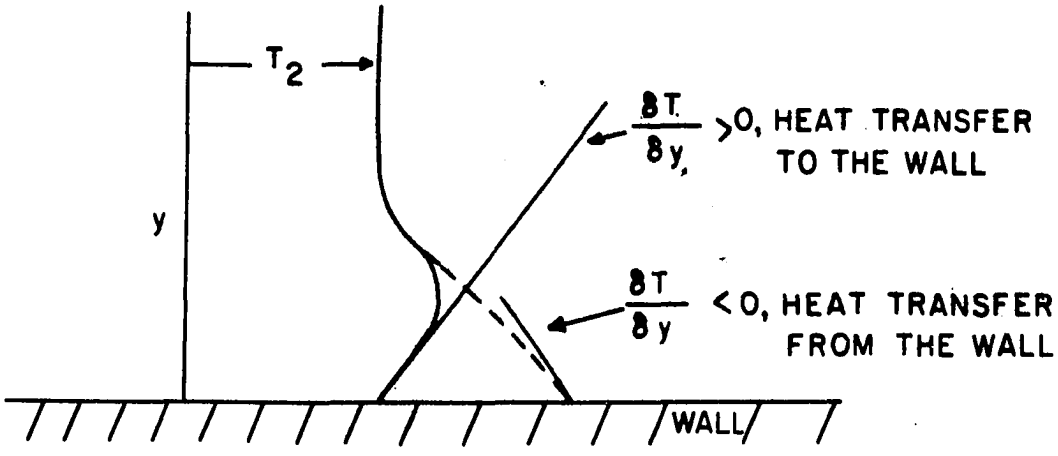

Figure 3B. Temperature profiles in the boundary layer in high-speed flow involving heat transfer to or from the wall

adiabatic wall temperature. The adiabatic wall temperature is not necessarily the free-stream stagnation temperature. Its value depends on the relation between the rate at which viscous dissipation increases the temperature in the boundary layer and the rate at which heat is conducted out of the viscous region toward the free stream. Thus T_{aw} depends on the Prandtl number. In practice a recovery factor r is defined which relates T_{aw} to T_2 and T_2°.

$$r = \frac{T_{aw} - T_2}{T_2^\circ - T_2} \qquad \text{Eqn. 17.}$$

The recovery factor for gases has been found to be related to the Prandtl number as follows:

$$r = \sqrt{Pr} \qquad \text{Eqn. 18.}$$

Boundary layer temperature profiles for flows involving heat transfer to or from the fluid are shown in Figure 3B. For the case shown where $(\partial T/\partial y)>0$ at the wall, it is noted that by Equation 16 the heat transfer is negative with respect to the fluid (positive with respect to the wall), yet the wall temperature is greater than the free-stream temperature T_2. Therefore, for high-velocity flows involving heat transfer, the heat-transfer coefficient for heat transfer to the wall is not based on the difference between the free-stream temperature and

the wall temperature. For high-velocity flow one definition of the heat-transfer coefficient is

$$h_i = \frac{q}{i_{aw} - i_w} \qquad \text{Eqn. 19.}$$

where q is the heat transfer rate to the wall and $(i_{aw} - i_w)$ is the enthalpy difference with the enthalpies evaluated at T_{aw} and T_w. Note that this definition accounts for variation of specific heat with temperature.

For low-velocity constant-property laminar boundary layers on a flat plate the local skin-friction coefficient and local Nusselt number can be accurately determined by the well-known relations:

$$C_f = \frac{.664}{(Re_2)^{1/2}} \qquad \text{Eqn. 20.}$$

$$Nu = 0.332\ (Re)^{1/2}\ (Pr)^{1/3} \qquad \text{Eqn. 21.}$$

A method outlined by Eckert (30) permits these equations to be applied to high-velocity air flow over a flat plate of uniform surface temperature. Eckert indicates that this method (referred to as the reference enthalpy method) is applicable to a wide range of temperature. In this technique the Nusselt number in Equation 21 is based on the heat-transfer coefficient defined in Equation 19, and temperature-dependent properties

in Equations 18 and 21 are introduced at the reference enthalpy i* given by:

$$i^* = i_2 + 0.5(i_w - i_2) + 0.22\,(i_{aw} - i_2) \qquad \text{Eqn. 22.}$$

Similarly, C_f is determined at a Reynolds number in which temperature-dependent properties are evaluated at i*.

Another work frequently referenced in the literature pertaining to laminar boundary layers in high-speed flow is that of Van Driest (27). Reference 27 presents in graphical form the various boundary-layer papameters along with skin-friction and heat-transfer coefficients for flat-plate flow as a function of Mach and Reynolds numbers and the ratio of wall to free-stream temperature for fluids with a constant Prandtl number of 0.75. Van Driest's results were determined from theoretical considerations using Sutherland's viscosity law. The curves in reference 27 are particularly useful in visualization of the effect of various flow parameters on the laminar boundary layer on a flat plate.

Summary

Interactions between an oblique shock wave and a laminar boundary layer can be classified into three categories.

1. Pure-laminar interactions involving no boundary layer separation. (Incident shock wave too weak to cause separation.)

2. Pure-laminar interactions involving boundary layer separation. (Incident shock wave strong enough to cause flow separation but not strong enough to cause transition to turbulent boundary layer flow.)

3. Transitional interactions. (Incident shock wave strong enough to cause separation and transition to turbulent boundary layer flow.)

A large portion of the experimental and theoretical work has been concerned with the adiabatic pure-laminar interaction involving separation (category 2 above) with emphasis on the study of the flow pattern and skin-friction and pressure distribution in the interaction region. The dimensionless parameters governing the nature of the adiabatic interaction of a laminar boundary layer and an incident shock wave are the Mach and Reynolds numbers and the pressure coefficient describing the overall pressure rise associated with the incident-reflected shock waves.

From the work reviewed in the previous sections it appeared that the interaction flow pattern for the laminar boundary-layer shock-wave interaction involving heat transfer would be qualitatively similar to that occurring in the adiabatic interaction. Although there is some indication that the extent and stability of the interaction involving flow separation are affected by heat transfer, flow separation and reattachment would be expected to occur for incident shock strengths above a certain value. It appeared that the incipient separation pressure coefficient could be predicted by Equations 4 and 6 for interactions involving heat transfer.

Table 1 is a summary of some investigations of heat transfer in supersonic laminar separated and reattaching flow regions. The results of these studies projected to the pure-laminar shock-wave boundary-layer interaction involving flow separation indicate that compared to heat-transfer rates for undisturbed flow, lower heat-transfer rates should occur in the region of separated flow while rates in the reattachment zone and downstream of it would be expected to be higher than local undisturbed-flow heat-transfer rates. The increased reattachment rates are strongly indicated from the results of the investigation by Rom and Seginer (16) while a decrease in average or local heat-transfer rates in the separated region is evident in several of the investigations summarized in Table 1.

Table 1. Summary of some investigations of heat transfer in laminar supersonic separated and reattachment flow regions

Investigation	Geometry	Separated Region		Reattachment Region
		$\bar{q}'_s/\bar{q}_{fps}$	Remarks	
Larson (12) (Experimental)	Axially-symmetric and two-dimensional models with cavities down stream of leading edge	0.56	Independent of Mach and Reynolds numbers	Relatively high local heat-transfer rates measured in reattachment zone below dividing streamline
Bogdanoff and Vas (10) (Experimental)	Cone model with cavity downstream of nose	0.5	Independent of Reynolds number	
	Compression corner model	Approx. 1.0	Minimum local $q'/q_{fp} \doteq 0.50$	Heat-transfer rates approximately 1.6 times local flat-plate rates
Miller et al. (14) (Experimental)	Compression corner model	0.60 to 0.80		

Table 1. (continued)

Investigation	Geometry	Separated Region		Reattachment Region
		$\bar{q}'_s/\bar{q}_{fps}$	Remarks	
Rom and Seginer (16) (Experimental)	Backward-facing step model			Heat-transfer rates were up to seven times local flat-plate rates. Results strongly dependent on Reynolds number. Trend extended downstream of reattachment zone.
Chapman (24) (Theoretical)	Leading edge separation	0.56	Independent of Mach and Reynolds number	

EXPERIMENTAL INVESTIGATION

Scope of the Investigation

In view of the fact that considerable previous work has been concerned with the flow characteristics of pure-laminar shock-wave boundary-layer interactions involving flow separation, it was decided that the present investigation should be limited to the study of heat transfer in interactions of this type. Since interactions involving flow separation have a marked effect on the flow near the surface on which the interaction occurs, it appeared that this interaction would be of most interest in a heat-transfer investigation.

Shock-wave boundary-layer interactions similar to those which would occur under aerodynamic heating conditions would necessarily require conditions where the surface temperature is less than the adiabatic wall temperature. Such conditions can be obtained in a shock tube. One aspect inherent to the use of a shock tube for aerodynamic heat-transfer studies which will be reviewed in a subsequent section is that relatively cold models can be subjected to high-temperature supersonic flow during testing. Thus the shock tube appeared to be a suitable facility for experimentally investigating heat-transfer rates in shock wave boundary-layer interactions. One additional aspect of shock-tube flow is that the shock tube generates flows within a limited Mach number range while the Reynolds number can be varied with relative ease over a

reasonably wide range. These facts suggested that any investigation utilizing a shock tube should be conducted at a given Mach number with a variable Reynolds number. This appeared especially appropriate since the nature of shock-wave boundary-layer interactions depends strongly on Reynolds number.

Thus, it was the specific purpose of this investigation to study primarily by experimental means the heat-transfer rates in pure-laminar separated-flow shock-wave boundary-layer interactions occurring at a given Mach number and over a range of Reynolds number. The experimental phase of this investigation was carried out in the Iowa State University shock tube using flat-plate shock-generator models like those shown in Figure 1A. Details of this investigation and the results are presented in the following sections.

Shock Tube

High-velocity high-temperature flow can be generated with relative ease in a shock tube (31, 32). However, a basic limitation associated with using the shock tube for aerodynamic testing lies in the short testing times available.

Figure 4A shows schematically the chamber (high-pressure section) and the channel (low-pressure section) of a constant-area shock tube. Initially the chamber and channel are separated by a diaphragm. The chamber is pressurized with a gas (referred to as the driver gas) while the pressure of the test gas in the channel, usually air, is reduced to a

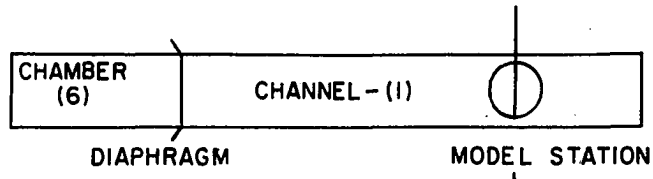

A. Initial conditions

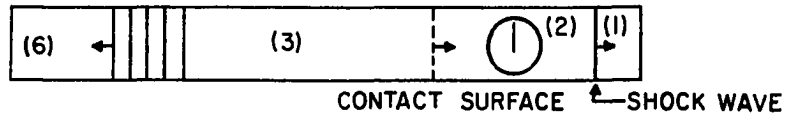

B. Conditions at $t = t_1$

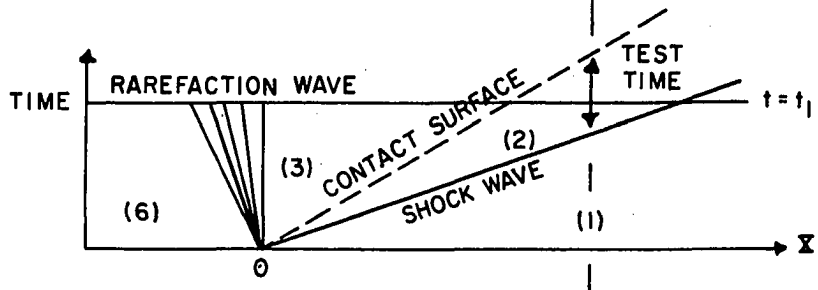

C. X - t diagram

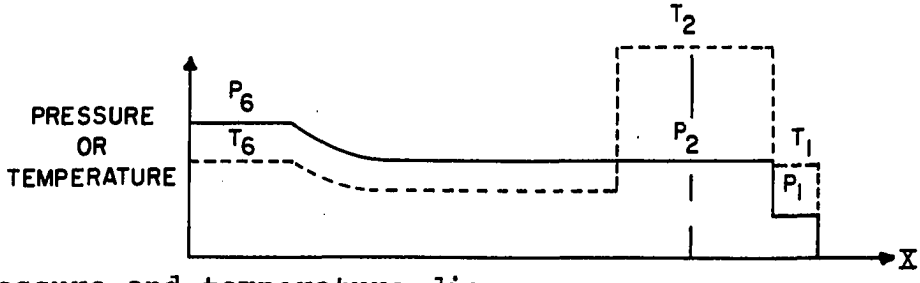

D. Pressure and temperature diagram

Figure 4. Ideal shock-tube flow

relatively low value. Rupturing the diaphragm initiates a normal shock wave which propagates into the stationary test gas in the channel while a rarefaction wave moves in the opposite direction. The passage of the shock wave through the stationary gas in the channel compresses the gas and sets it in motion in the direction of travel of the shock wave. The velocity of the compressed gas may be either subsonic or supersonic depending on the velocity of the normal shock and the sonic velocity in the undisturbed test gas. The contact surface between the expanding driver gas and the test gas moves down the channel but at a lower velocity than the shock wave. Thus a quantity of compressed test gas occupies the region between the shock wave and the contact surface. This is region 2 in Figure 4B and is the region useful for aerodynamic testing. Ideally it is a region of uniform velocity and uniform thermodynamic properties.

Figure 4B shows the relative positions of the normal shock wave and the contact surface at a time t_1 after the diaphragm has been ruptured. At this time the test gas is flowing by the model station. The X-t diagram describing ideal shock tube flow is shown in Figure 4C. The testing time is the time interval between the arrival of the normal shock wave and the arrival of the contact surface at the model station. This time is of the order of a few milliseconds or less depending on the flow conditions and the channel length. Figure 4D is a diagram of the pressure and temperature along the shock tube at time t_1

corresponding to the wave positions shown in Figure 4B.

The pressure ratio P_2/P_1 is ideally related to the initial chamber pressure (denoted herein as P_6) and the initial channel pressure P_1 by the following relation given by Glass and Patterson (31). Constant specific heats are assumed.

$$\frac{P_1}{P_6} = \frac{1}{P_2/P_1}\left[1 - \left(\frac{P_2}{P_1} - 1\right)\sqrt{\frac{\beta_6 E_{16}}{\alpha_1 \frac{P_2}{P_1} + 1}}\right]^{\frac{1}{\beta_6}} \qquad \text{Eqn. 23.}$$

where $\beta_6 = \frac{\gamma_6 - 1}{2\gamma_6}$

$$\alpha_1 = \frac{\gamma_1 + 1}{\gamma_1 - 1}$$

$$\gamma = \frac{c_p}{c_v}$$

$$E_{16} = \frac{(c_v T)_1}{(c_v T)_6}$$

In each of these equations the subscript 6 refers to the driver gas and the subscript 1 refers to the test gas at initial channel conditions.

The shock wave Mach number M_s is given as

$$M_s = \left[\beta_1 \left(1 + \alpha_1 \frac{P_2}{P_1}\right)\right]^{1/2} \qquad \text{Eqn. 24.}$$

where M_s is the shock speed divided by the sonic velocity in region 1. The temperature ratio across the shock wave may be written as

$$\frac{T_2}{T_1} = \frac{\frac{P_2}{P_1}(\alpha_1 + \frac{P_2}{P_1})}{1 + \alpha_1 \frac{P_2}{P_1}} \qquad \text{Eqn. 25.}$$

The Mach number in region 2 is given by

$$M_2 = \sqrt{\frac{T_1}{T_2}} \left(\frac{P_2}{P_1} - 1\right) \sqrt{\frac{2\gamma_1}{(\gamma_1 + 1)(P_2/P_1) + (\gamma_1 - 1)}}$$

Eqn. 26.

In this investigation room-temperature helium was used as the driver gas and the test gas was air initially at room temperature. For $T_1 = T_6$, the ratio E_{16} in Equation 23 is relatively low. Therefore for a given P_6/P_1, helium used as the driver gas yielded a stronger normal shock wave than would have been obtained using a gas with a higher molecular weight. Inspection of Equations 23, 24, 25, and 26 reveals that M_2 and M_s are both functions only of P_6/P_1 when $T_6 = T_1$, constant specific heats are assumed, and a given driver gas is used. Figure 5A shows M_s and M_2 as a function of P_6/P_1 for helium driving air and $T_6 = T_1$. The ratios P_2/P_1 and T_2/T_1 as a

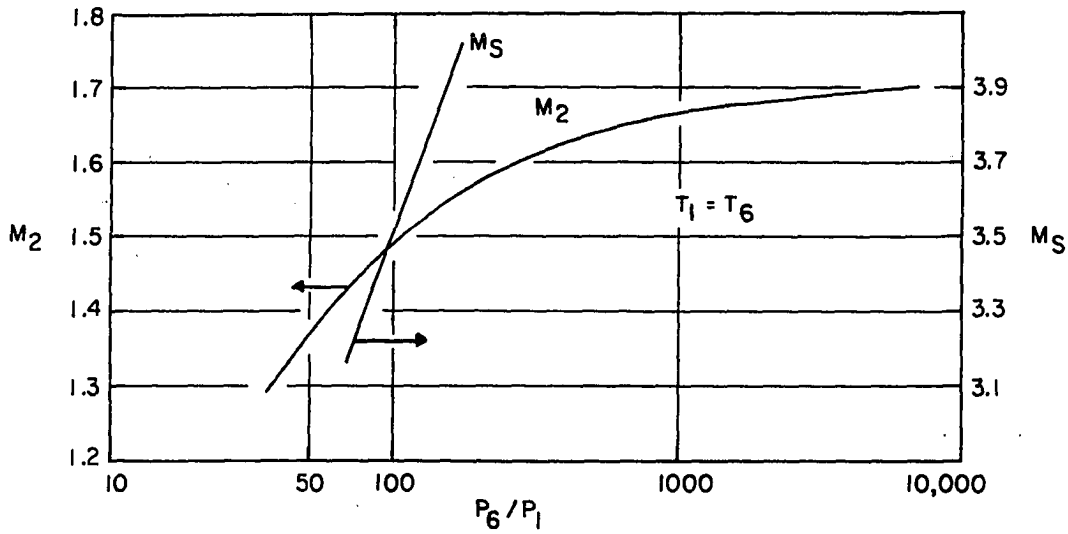

Figure 5A. Mach numbers in shock-tube flow for helium driving air

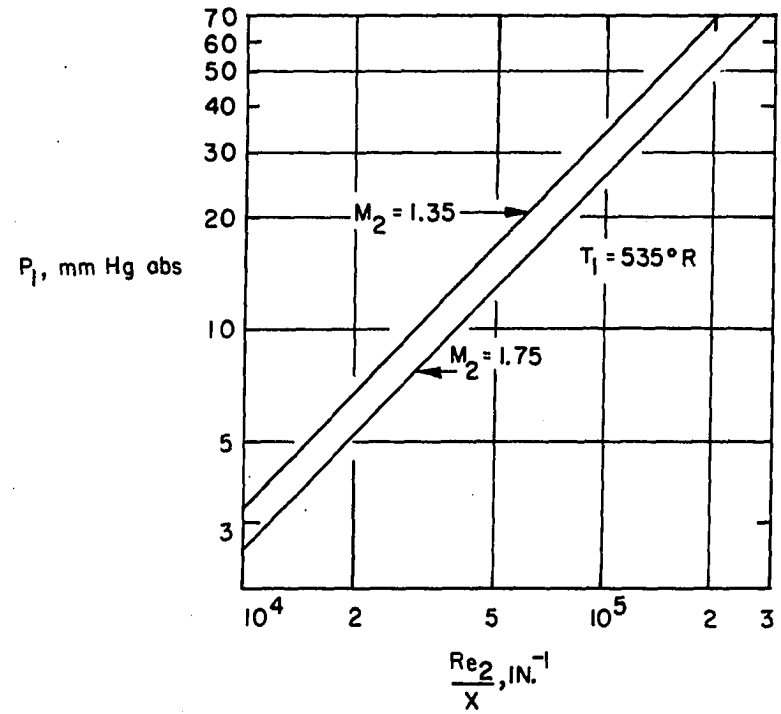

Figure 5B. Shock-tube Reynolds number

function of M_s can conveniently be determined for air by direct use of normal shock tables.

The Reynolds number per unit length in region 2 is

$$\frac{Re_2}{x} = \frac{V_2 \rho_2}{\mu_2} = \frac{V_2 \; P_2}{\mu_2 \; R \; T_2} = \frac{V_2}{\mu_2 R}\left(\frac{P_2}{P_1}\right)\left(\frac{T_1}{T_2}\right)\left(\frac{P_1}{T_1}\right) \qquad \text{Eqn. 27.}$$

Because P_2/P_1 and T_2/T_1 are functions only of M_s (and therefore M_2, since M_s and M_2 are seen in Figure 5A to be dependent), the Reynolds number at any M_2 depends on P_1 and T_1. Figure 5B shows a plot of P_1 and the Reynolds number per inch in region 2 for two values of M_2. T_1 was taken as 535 °R (room temperature) for this figure.

As previously noted, region 2 is the region in shock tube flow which is useful for aerodynamic testing. Region 2 flow passing the model station provides the test conditions and thus region 2 flow conditions become the free-stream conditions with respect to the model. For this reason the subscript 2 is used to designate the free-stream properties in this investigation. Figure 5 provided a basis for the selection of the free-stream Mach and Reynolds numbers for this investigation as outlined in the next section.

Shown in Figure 6 is a schematic diagram of the Iowa State University shock tube and the associated instrumentation used in this investigation. The tube is 3 by 6 inches in cross-section and is 38 feet long. Since there is a departure from

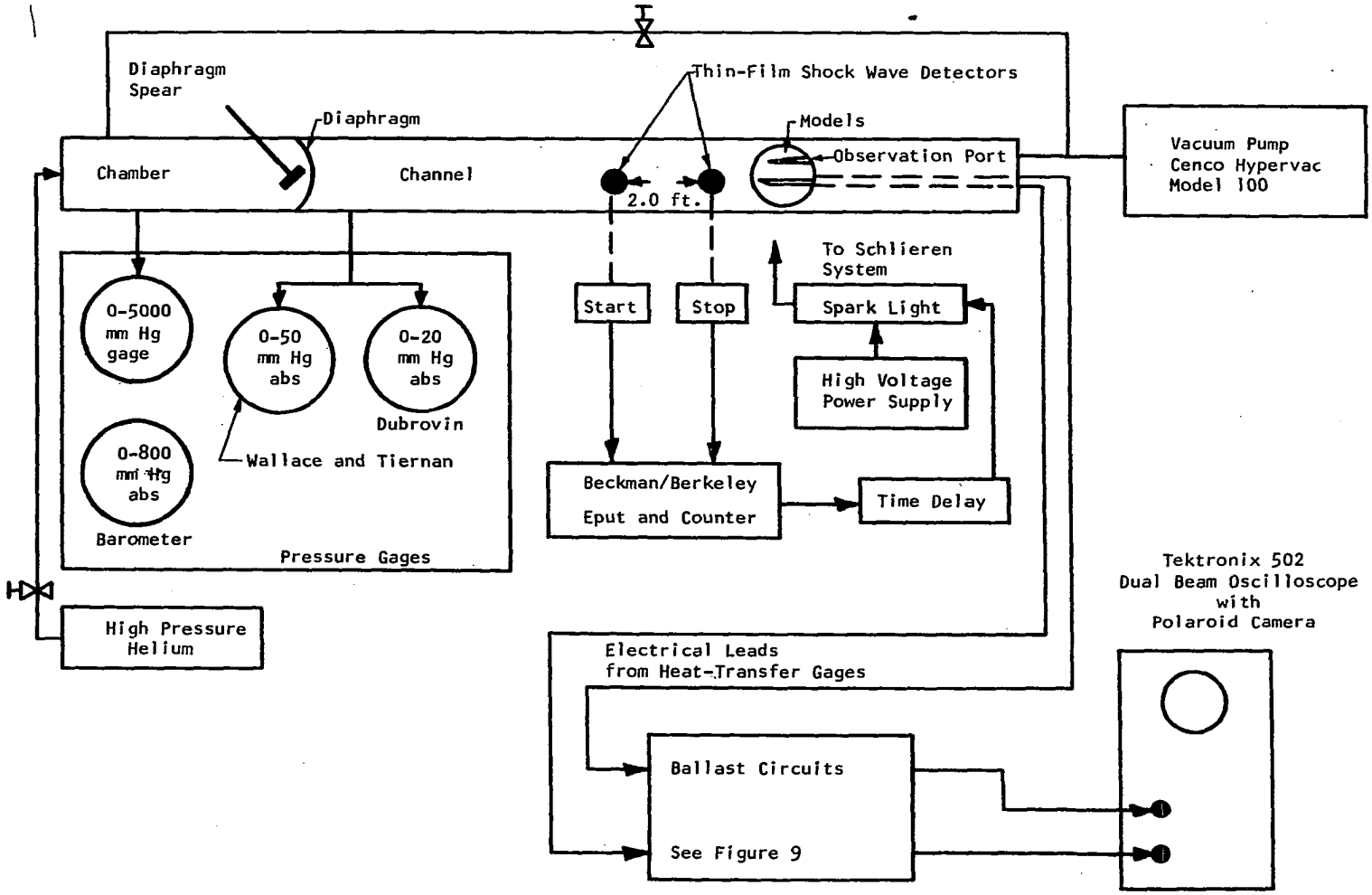

Figure 6. Schematic diagram of the Iowa State University shock tube

ideal shock-tube relations in real shock-tube flow, it is necessary to measure the velocity of the normal shock wave and in turn use this velocity to determine M_s. The normal shock velocity is determined in the Iowa State University shock tube by platinum thin-film sensing devices located two feet apart just upstream of the model station. See Figure 6. The electrical output of these sensing devices is fed through amplifiers into the Beckman-Berkeley counter which records the time interval in microseconds for the passage of the normal shock between the two sensing devices. A Schlieren photographic system is used to photograph the flow pattern around models mounted at the model station. Photographic illumination is obtained by means of a spark light and half-size pictures are produced on 3000 speed 4 x 5 Polaroid film. The electrical signal that stops the counter is passed into a time delay circuit which can be set to trigger the spark light at the desired time. The knife edge of the Schlieren system was set parallel to the free-stream flow for the Schlieren photos taken during the course of this investigation.

Selection and Determination of Test Parameters

Mach and Reynolds numbers

The governing factor in the selection of the Mach number and the range of Reynolds number in this investigation was the shock tube chamber pressure P_6. The practical upper limit for the chamber pressure of the ISU shock tube at the time of this

investigation was approximately 5800 mm Hg abs. Since M_2 is a function of P_6/P_1 (Figure 5A), the value of P_1 corresponding to the maximum permissible value of P_6 depends the value of M_2 desired, i.e., for a fixed P_6, increasingly higher values of M_2 require increasingly lower values of P_1. Therefore, since Reynolds number per inch in region 2 is proportional to P_1 at a fixed T_1 (disregarding the small Mach number effect seen in Figure 5B), increasing the Mach number with a fixed P_6 effectively reduces the Reynolds number range.

To obtain a reasonably high Mach number in the range available and a reasonably wide range of Reynolds number, a shock Mach number of 3.5 was selected. According to Figure 5B this corresponded to a Mach number in region 2 of approximately 1.5 and a value of P_6/P_1 of about 100. This indicated that a Mach number of 1.5 could be obtained for values of P_1 as high as 58 mm Hg abs. In actual shock tube operation, however, it was found that it was not possible to obtain a Mach number of 1.5 for channel pressures above about 32 mm Hg abs. It was felt that this was due primarily to the manner in which the shock tube diaphragms ruptured. Figure 5B shows that the Reynolds number corresponding to P_1 = 32 mm Hg abs is about 11×10^4 per inch. This then was the maximum Reynolds number available at the test Mach number of approximately 1.5.

Appendix A presents sample calculations which include the determination of the parameters M_2, T_2, and V_2 which are determined solely by M_s and T_1. Gas tables (33) were used for these

calculations. For $M_s = 3.5$, M_2 was calculated to be 1.52. It is important to note that since shock tube models remain at essentially the temperature T_1 during testing, the ratio of surface temperature, T_w, to free stream temperature for a fixed T_1 is a function of M_s. The ratio T_w/T_2 corresponding to $M_2 = 1.52$ and $T_1 = 535°R$ is 0.335.

Incident shock strength

Values of the flow deflection angle θ for the incident shock-wave generating wedge (Figure 1) were selected with the intention of inducing pure-laminar separation. Interactions for two values of θ, 3° and 5°, were studied in the course of this investigation.

Figure 7 shows the pressure coefficients corresponding to each of the angles for $M_2 = 1.52$. Also shown are calculated values of the pressure coefficient C_{pi} which depends on Re_o, the Reynolds number based on free-stream properties and x_o.

For comparison, C_{pi} was calculated using Equations 4 and 9 which are taken from references 9 and 26, respectively. C_{pi} was taken as 2 C_{ps} (see Equation 6). The skin-friction coefficient C_{fo} in Equation 4 was evaluated from Equation 20 using Eckert's reference enthalpy method and the region 2 flow conditions dictated by $M_2 = 1.52$ and $T_1 = 535°R$. Evaluation of C_{ps} by Equation 9 required use Van Driest's Figure 3, reference 27, which gives the skin-friction coefficient for supersonic flow at various ratios of wall to free-stream temperature. Figure 7

shows that the two methods give similar C_{pi} values. Boundary-layer separation should occur in shock-wave boundary-layer interactions for interaction condition lying above the C_{pi} curves. Below these, boundary layer separation would not be expected.

In the absence of better information, the approximate upper limit for pure-laminar interactions is shown as three times the plateau pressure coefficient. This was based on the previously discussed experimental work of Chapman et al. (8) for adiabatic interactions. Equations 5 and 10 gave almost identical results for C_{pp}. Therefore, a single curve is shown in Figure 7 for 3 C_{pp}. The region above C_{pi} and below 3 C_{pp} in Figure 7 was considered as the approximate pure-laminar separation region. Reference will be made to this figure in subsequent discussion.

Variation of test parameters with counter time

Figure 26, Appendix A, shows the variation in some test parameters as a function of the time in microseconds required for the normal shock in shock-tube flow to pass between the two shock-wave detectors shown schematically in Figure 6. This corresponds to the time that the Beckman-Berkeley counter would record. A Mach number of 1.52 is seen to correspond to a counter time of 502 microseconds. Experience in the operation of the ISU shock tube indicated that in 500 microsecond range counter times were, with care, repeatable within ± 10

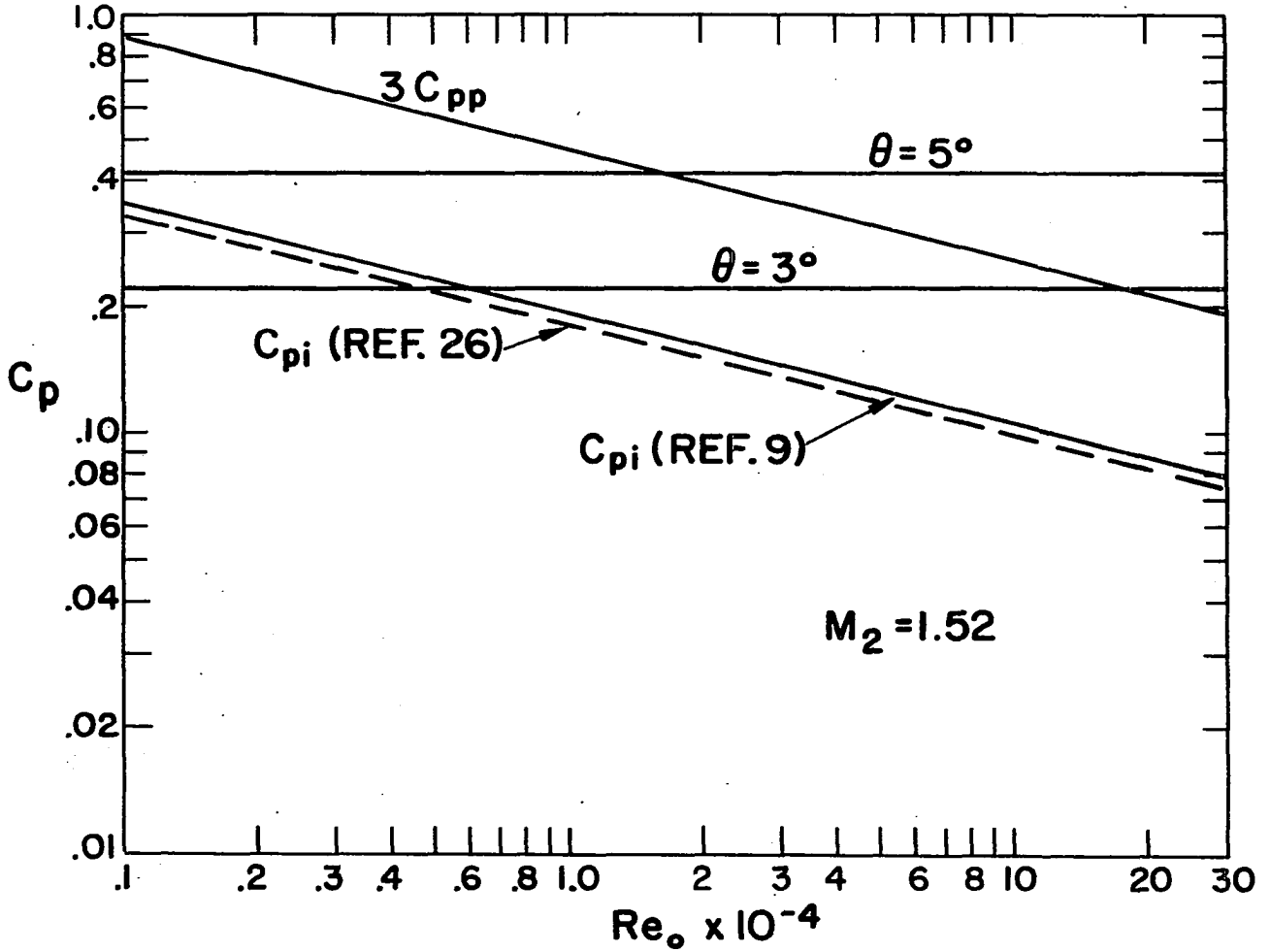

Figure 7. Various pressure coefficients as a function of Re_o

microseconds. Figure 26 indicates that counter times ranging from 490 to 510 microseconds correspond to $M_2 = 1.52 \pm .02$. Data taken in this investigation were considered acceptable for counter times within this range.

Also shown in Figure 26 is the theoretical variation of free-stream temperature, T_2, with counter time.

Model Design

Figure 8 shows the models used in this investigation mounted in the shock tube. The models were milled from mild steel plate and were polished with fine abrasive paper for final finish. The leading-edge included angle (7°) on the flat plate was chosen to obtain an attached shock wave, and the flat plate was machined to receive the pyrex glass insert which served as a backing material for the thin-film heat-transfer gages (see next section). The models completely spanned the 3-inch tube width except for a small clearance on each side. The shock-generating wedge was supported by a thin strut attached to the upper surface of the tube. The flat-plate mounting bracket was designed to permit the test plate to be moved in the direction of the longitudinal axis of the shock tube. The reason for this is explained in a following section. Brackets supporting the models were carefully machined to obtain proper alignment with respect to each other and the axis of the shock tube. The shock-generator flow-deflection angles, 3° and 5°, were determined after the models

Figure 8. Models mounted in the shock tube
(photo is approximately full size)

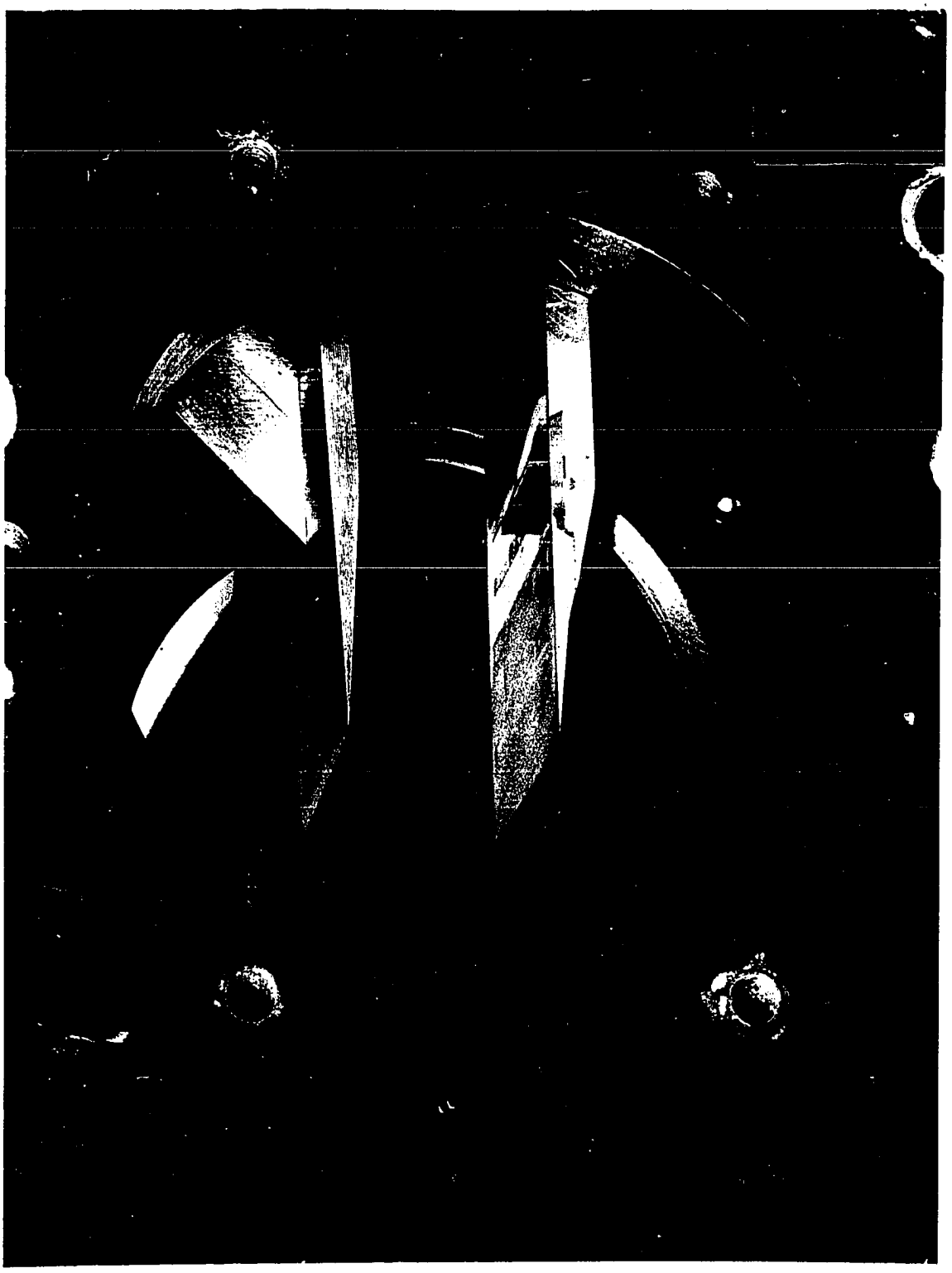

were mounted by measuring these angles on Schlieren photographs. It is estimated that the angles were within ±0.2° of the stated values.

Heat-Transfer Gages

An accepted method for measuring heat-transfer rates to shock-tube models for low heat-transfer rates is the thin-metallic-film technique (34, 35, 36, 37).

This method involves depositing an extremely thin film of metal (usually platinum) on an electrically-insulating backing material which in turn becomes an integral part of the model. The thin-film acts as the temperature sensitive element in an electrical-resistance thermometer circuit and provides a means by which the surface temperature of the backing material may be measured as a function of time. The surface-temperature time history can then be used to determine heat-transfer rates as a function of time. Film thicknesses in the order of 40 microinches can be obtained, and, as a result, the films have negligible heat capacitance (37, 38). The time required for the diffusion of heat through the films is of the order of 10^{-10} seconds (37, 38). Figure 9 shows the voltage-sensitive operating circuit used in this investigation for heat-transfer measurement.

The thin films used in this investigation were obtained by using Hanovia 05-X Liquid-Bright platinum purchased from Englehard Industries, Newark, New Jersey and were deposited

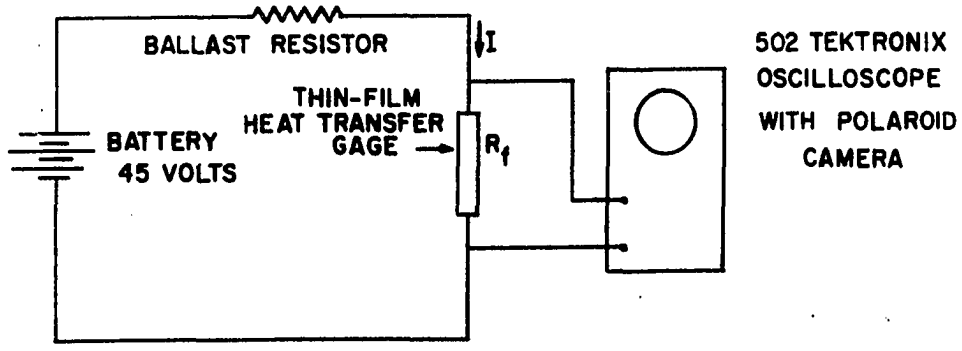

Figure 9. Thin-film heat-transfer gage operating circuit

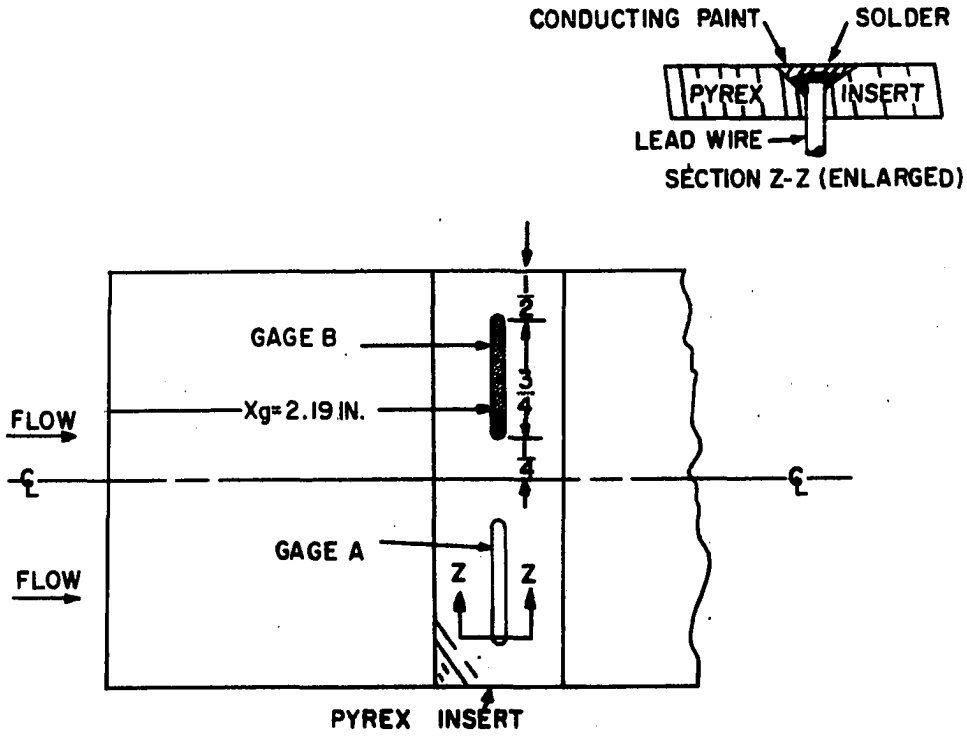

Figure 10. Top view of flat-plate model

on pyrex glass inserts cut and ground to fit into the flat-plate model. Figure 10 shows the positions where gages were located on the flat-plate model. The gages were located 1/2 inch from the edge of the plate to eliminate measuring heat transfer in the region where the boundary layer on the plate might be influenced by the presence of the shock-tube wall. Gages were positioned at two locations primarily to check the uniformity of heat transfer across the plate. The means by which gages at a fixed location from the leading edge were used to survey the interaction region of shock-wave boundary-layer interactions is explained in a following section.

Also shown in Figure 10 is a cross-section illustrating the technique used to make electrical connections to the thin films. Holes were first drilled through the 1/8-inch-thick pyrex insert at the ends of the intended gage locations. Each hole was countersunk from the top surface and subsequently the countersunk area was flame polished. Liquid-Bright platinum was painted between the holes and into the countersunk areas to form the gages. The insert was fired at 1200 °F in a furnace for 15 minutes to drive off the organic vehicle in the platinum deposited on the pyrex. An additional coat of platinum was applied and the firing process was repeated. Soldering to the thin films involved inserting wires tinned with solder into the holes from the under surface and heating the assembly to 550 °F in a furnace for a short period. Immediately on removal of the assembly from the furnace short

lengths of small-diameter rosin-core solder were dropped into each of the countersunk areas and firm solder connections resulted. The solder which protruded above the surface was trimmed off and the remaining cavities were filled with electrical conducting paint. This served to form a smooth upper surface and rendered ineffective the film not on the flat upper surface of the insert. The insert was fitted into the recess in the flat-plate model so that there was negligible surface discontinuity. Final smoothing of the metal-to-glass joints was obtained by coating the joints with lacquer-base auto-body putty and sanding off the excess with fine abrasive paper. Holes and slots machined in the metal portion of the model were provided to accomodate the lead wires from the thin-film gages.

During the course of this investigation two separate pyrex insert gage assemblies (a total of four gages) were used. These gages were designated as gages A_1, B_1, A_2 and B_2 corresponding to the gage locations in Figure 10.

Determination of Heat-Transfer Rates from Gage Output

Determination of heat-transfer rates from surface-temperature history involves treating the backing material on which the thin-film gages are deposited as a semi-infinite slab initially at uniform temperature. Hence the thickness of the backing material must be chosen such that the time

required for heat diffusion through the material is longer than the shock-tube testing time.

The one-dimensional unsteady state heat conduction equation for an homogeneous isotropic solid is

$$\frac{\partial \phi(y, t)}{\partial t} = \frac{k \partial^2 \phi(y, t)}{\rho c_p \partial y^2}$$

where $\phi(y, t) = T - T_o$ and T_o is the initial uniform temperature of the solid. The initial and boundary conditions necessary for solution of the above equation for the conditions under consideration are

$$\phi(y, 0) = 0 \qquad y \geq 0$$

$$\lim_{y \to \infty} \phi(y, t) = 0 \qquad t \geq 0$$

$$\phi(0, t) = \phi(t) \qquad t > 0$$

The rate of heat transfer in the solid is

$$q(y, t) = - \frac{k \partial \phi(y, t)}{\partial y}$$

Solution of the above equations for the heat transfer rate per unit area at $y = 0$ (the surface) yields

$$q(0, t) = q(t) = \frac{\Gamma}{\sqrt{\pi}}\left[\frac{\phi(t)}{\sqrt{t}} + \frac{1}{2}\int_0^t \frac{\phi(t) - \phi(\tau)}{(t - \tau)^{3/2}}\, d\tau\right] \quad \text{Eqn. 28.}$$

where $\Gamma = \sqrt{k\rho c_p}$, τ is a variable of integration, and $\phi(t)$ is an arbitrary function (15, 36). Use of a large ballast resistor in the thin-film operating circuit in Figure 9 maintains the electrical current in the circuit essentially constant when the film resistance R_f changes as a result of surface temperature change. Therefore, the film voltage change is

$$E(t) = I\Delta R_f$$

where

$$\Delta R_f = R_{fo}\alpha(T - T_o) = R_{fo}\alpha\phi(t)$$

for small changes in surface temperature. Combining the two above equations gives

$$E(t) = I\, R_{fo}\alpha\phi(t) = E_{fo}\alpha\phi(t)$$

or

$$\phi(t) = \frac{E(t)}{E_{fo}\alpha} \quad \text{Eqn. 29.}$$

Substitution of Equation 29 into Equation 28 yields

$$q(t) = \frac{\Gamma}{\alpha E_{fo}\sqrt{\pi}}\left[\frac{E(t)}{\sqrt{t}} + \frac{1}{2}\int_{o}^{t}\frac{E(t) - E(\tau)}{(t-\tau)^{3/2}}\,d\tau\right] \qquad \text{Eqn. 30.}$$

Thus the film voltage change is related to the heat-transfer rate. In the experimental phase of this investigation a dual beam model 502 Tectronix oscilloscope with an oscilloscope camera using 3000 speed type 47 Polaroid film was used to simultaneously record the voltage change across the two thin-film gages on the flat-plate model.

Calibration of the thin-film heat-transfer gages is necessary since it has been shown that the deposition of the platinum film on the pyrex may change both the properties of the film and the pyrex (34, 36). The method developed by Skinner (39) was used to determine Γ. Details of this method and the method by which α in Equation 30 was determined are presented in Appendix C.

Determination of heat-transfer rates through the use of Equation 30 necessarily involves using discrete values of thin-film voltage change read from the voltage-time trace. Therefore a numerical integration procedure is required to evaluate the integral in Equation 30. Integration procedures such as the trapezoid rule make accurate evaluation of the

integral difficult since the integral tends to infinity as τ approaches t. A method suggested by Crane[1] circumvents this difficulty. The method involves approximating the voltage-time trace by a piecewise-linear function determined by reading the voltage values from the voltage-time trace at times

$$t_i = i\Delta t \qquad i = 0, 1, 2, \cdots n$$

and integrating Equation 30 for this function. Appendix C shows the details of the integration and the resulting equation for q(t). Also included in Appendix C is the flow diagram for the computer program used to evaluate the equation. The computter program was written in EERIE language for the Iowa State University Cyclone digital computer.

Experimental Flat-Plate Heat Transfer

Before proceeding with the interaction heat-transfer investigation, it was decided that the heat-transfer rates for undisturbed laminar flat-plate flow should be measured and compared with accepted theory. This not only provided a check on the instrumentation but also provided a means by which the available testing time and the uniformity of the shock-tube flow could be observed.

Data were taken at a Mach number of 1.52 ± 0.02 and at various values of Reynolds number with only the flat plate

---

[1]Crane, R. L. Ames, Iowa. Reduction of equation for computer solution. Private communication. 1963.

mounted in the shock tube. Figure 11A shows typical heat-transfer gage response for gages at locations A and B for flat-plate flow as recorded by an oscilloscope camera. These traces which read from right to left were recorded for a run in which the free-stream Reynolds number based on x_g was 8.2×10^4. The steps exhibited by the traces at approximately two major scale divisions from the right-hand edge of the figure correspond to the arrival of the normal shock at the gage locations. After the step each trace indicates an additional uniform increase in gage voltage with time. The spots to the left of the vertical reticle are recordings of the initial film voltage E_{fo} for each gage before the run.

Figure 12A is a Schlieren photo taken for flat-plate flow 500 microseconds after the arrival of the region 2 test gases. The boundary layer is clearly visible on the upper surface of the plate.

Curves showing the heat-transfer rates determined from the traces in Figure 11A using the computer program are shown in Figure 13. Heat-transfer rates were calculated for times up to 800 microseconds using voltage values read at 20 microsecond intervals. Appendix B gives the details of the data reduction technique. It is seen in Figure 13 that the heat-transfer rate indicated by each gage became reasonably steady after about 300 microseconds and remained reasonably constant throughout the remainder of the 800 microseconds. In addition to calculating the heat-transfer rates at discrete points in

A. Traces for flat-plate flow

$Re_g = 8.2 \times 10^4$ $M_2 = 1.52$

Vertical sensitivity = 1 millivolt

Horizontal sensitivity = 100 microseconds

Traces read from right to left

Upper trace: Gage A_2

Lower trace: Gage B_2

B. Traces for flat-plate flow

$Re_g = 12.3 \times 10^4$ $M_2 = 1.52$

Vertical sensitivity = 1 millivolt

Horizontal sensitivity = 200 microseconds

Traces read from right to left

Upper trace: Gage A_2

Lower trace: Gage B_2

C. Traces for a shock-wave boundary-layer interaction

$Re_i = 4.95 \times 10^4$ $M_2 = 1.52$

$\theta = 5°$ $x_i/x = 1.2$

Vertical sensitivity = 1 millivolt

Horizontal sensitivity = 100 microseconds

Traces read from left to right

Upper trace: Gage A_2

Lower trace: Gage B_2

D. Traces for a shock-wave boundary-layer interaction

$Re_i = 14.9 \times 10^4$ $M_2 = 1.52$

$\theta = 5°$ $x_i/x = 0.6$

Vertical sensitivity = 5 millivolts

Horizontal sensitivity = 100 microseconds

Traces read from left to right and cross each other

Upper trace: Gage B_2

Lower trace: Gage A_2

Figure 11. Typical oscilloscope output traces from thin-film heat-transfer gages

(All sensitivities listed are per major scale division)

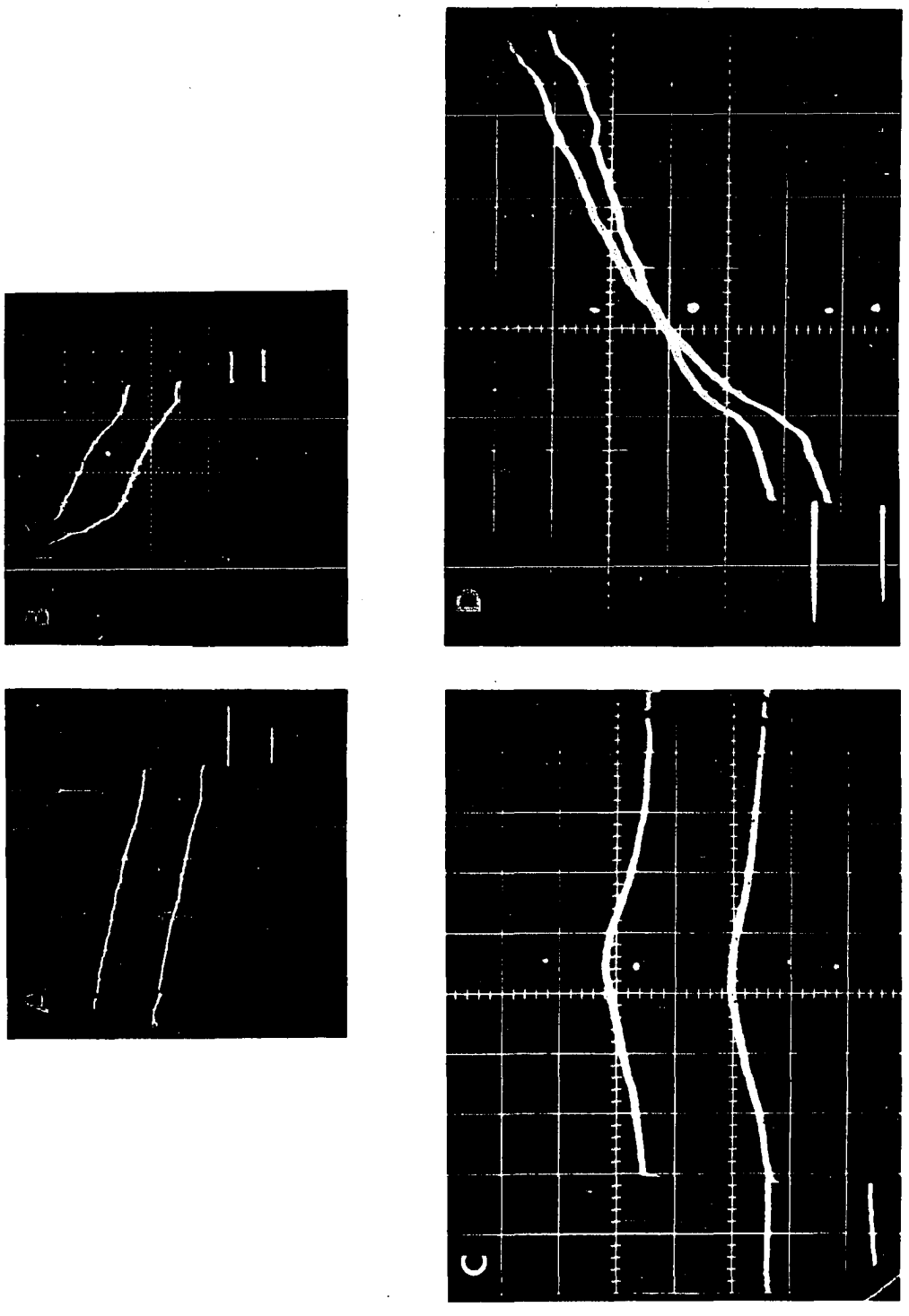
B
A
D
C

time, the computer program was written with an option which permitted the time-averaged heat-transfer rate and the standard deviation to be calculated for a specified fraction of the time span of the curve. The average heat-transfer rate for the flat portion of the two curves shown in Figure 13 differed by 3 per cent and the values of standard deviation were approximately 5 per cent of the corresponding steady-state average for each curve.

Flat-plate heat-transfer data taken at other Reynolds numbers gave results quite similar to those shown in Figure 13. Flat-plate data were taken using each of the four heat-transfer gages prepared for this investigation. The time required to reach steady heat-transfer rates ranged from approximately 100 to 300 microseconds. Most of the values of standard deviation were around 5 per cent of the corresponding average with a maximum of 10 per cent being observed. Appendix D gives an estimate of the uncertainty associated with the heat transfer measurement technique. It is estimated that the measured values are within 10 per cent of the true values.

Figure 14 shows the flat-plate heat-transfer results as indicated by the four heat transfer gages. The results presented correspond to values of initial channel pressure P_1 ranging from about 1 to 32 mm Hg abs. Counter times were in the range 490 to 510 microseconds. The results are presented in the coordinates shown to permit convenient comparison of

A. Flat-plate flow

t_f = 500 microseconds

$Re_g = 12.3 \times 10^4$

M_2 = 1.53

B. Shock-wave boundary-layer interaction

t_f = 600 microseconds

$Re_i = 11.4 \times 10^4$

M_2 = 1.52 $\theta = 3°$

$x_i/x = 0.7$

C. Shock-wave boundary-layer interaction

t_f = 600 microseconds

$Re_i = 19.4 \times 10^4$

M_2 = 1.51 $\theta = 3°$

$x_i/x = 1.2$

D. Shock-wave boundary-layer interaction

t_f = 500 microseconds

$Re_i = 8.3 \times 10^4$

M_2 = 1.54 $\theta = 5°$

$x_i/x = 0.8$

E. Shock-wave boundary-layer interaction

t_f = 500 microseconds

$Re_i = 14.9 \times 10^4$

M_2 = 1.52 $\theta = 5°$

$x_i/x = 1.2$

F. Shock-wave boundary-layer interaction

t_f = 700 microseconds

$Re_i = 14.9 \times 10^4$

M_2 = 1.52 $\theta = 5°$

$x_i/x = 1.2$

Figure 12. Typical Schlieren photographs (half-size)
(Flow is from right to left)

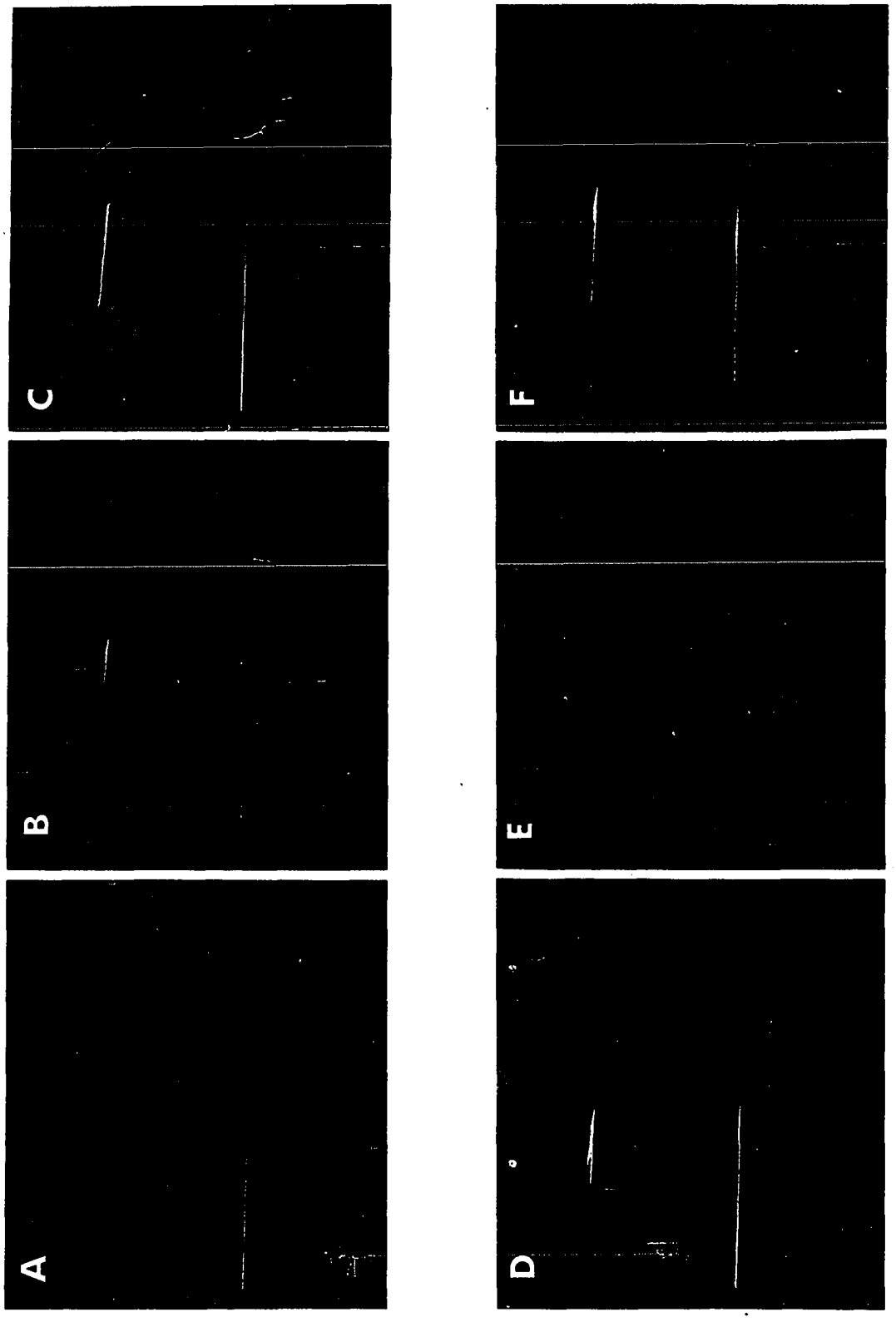
A
B
C
D
E
F

the experimental results with the prediction of Eckert's reference-enthalpy method. Sample calculations in Appendix A give the details of the calculations for Figure 14.

The experimental results in Figure 14 are seen to be in fairly good agreement with theory for reference state Reynolds numbers above about 5×10^4. This Reynolds number corresponds to a P_1 of about 4 mm Hg abs. Considerable effort was spent to discover the cause for the disagreement with theory for the data below this Reynolds number, but no satisfactory explanation was found. Therefore no data is presented for the interaction heat-transfer investigation for values of P_1 less than 4 mm Hg abs.

The results in Figure 13 and Figure 14 led to several conclusions for the reference Reynolds numbers range between 5×10^4 and 45×10^4. In addition to providing steady-state heat-transfer rates, the flat-plate flow was definitely laminar as indicated by the agreement with laminar theory in this range. Furthermore, inspection of the typical Schlieren photo for flat-plate flow shown in Figure 12A indicates that the boundary layer was laminar over the length of the plate visible. The acceptable agreement between the results indicated by all four gages (which were independently prepared and calibrated) and the observed agreement with theory gave confidence in the use of thin-film gages as a reasonably accurate technique for measuring heat-transfer rates for the flow conditions of this investigation.

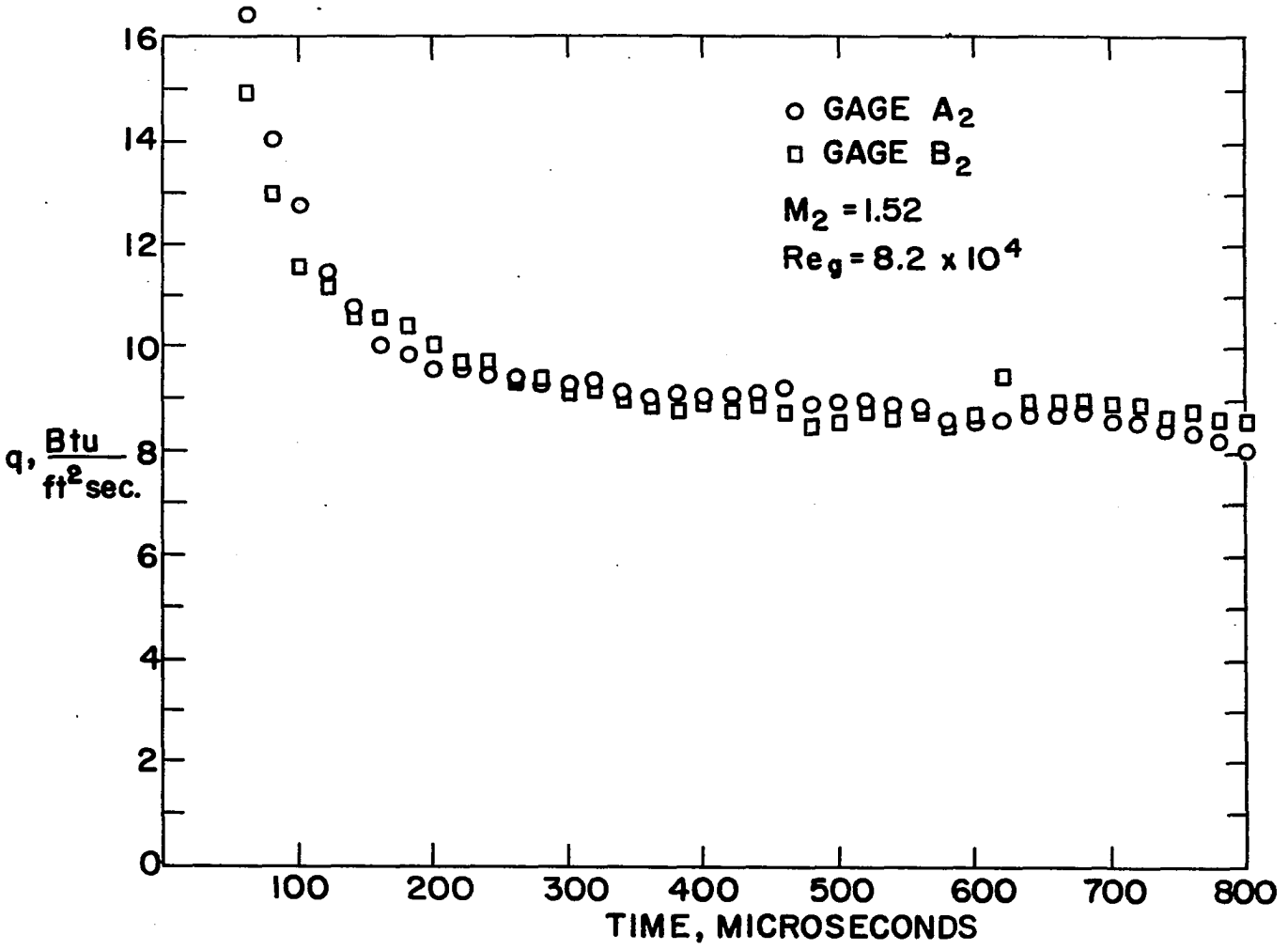

Figure 13. Heat-transfer rates corresponding to gage-response traces in Figure 11A for flat-plate flow

Steady flat-plate heat transfer rates were not obtained for region 2 flow beyond approximately 850 microseconds. This was not due to the arrival of the contact face between the driver and test gas since the output of a thin-film heat-transfer gage mounted at the stagnation point on a hemisphere model placed at the center of the tube cross-section indicated region 2 steady flow for approximately 1200 microseconds at $M_2 = 1.5$. The termination of the steady flat-plate heat transfer was due to flow choking below the flat-plate model. The effect of the choking is seen in Figure 11B which shows the response of gages A_2 and B_2 at an oscilloscope sweep rate of 200 microseconds per major scale division. At approximately 850 microseconds after the arrival of region 2 flow at the gage locations, the traces exhibit a sudden change in slope; a sudden rise in surface temperature indicating a sharp increase in heat-transfer rate. This was due to the formation of choking shock waves under the model and the propagation of these waves upstream to form a detached shock wave around the leading edge of the model. Because the high-temperature incoming flow passing through this shock wave experienced an additional temperature rise, the increased plate heat-transfer rates indicated after about 850 microseconds in Figure 11B resulted. The formation and propagation of the shock waves accompanying the choking was recorded by means of Schlieren photographs. The position of the wave at 500 microseconds after the start of flow can be seen in Figure 12A. Also

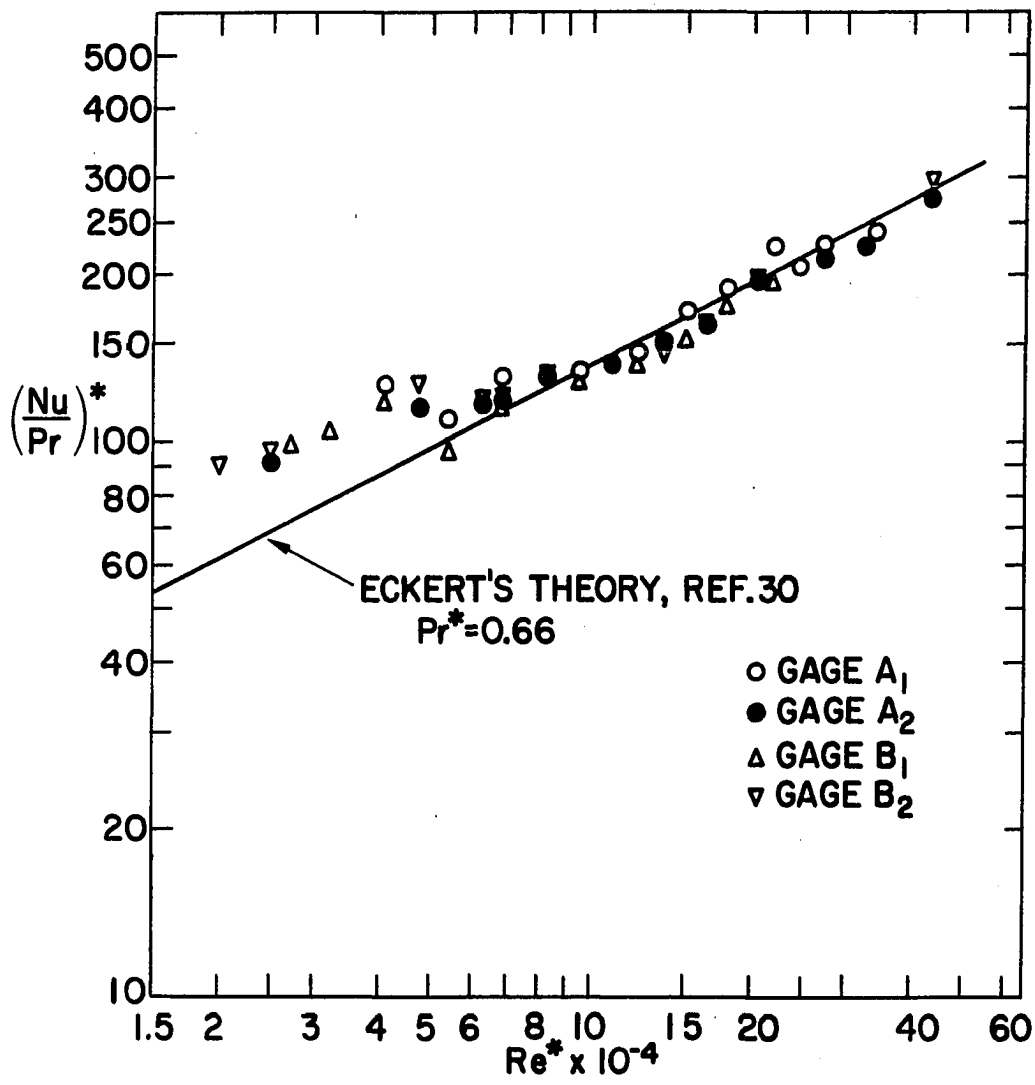

Figure 14. Comparison of theoretical and experimental results for flat-plate heat transfer

Figures 12B and 12F, which were taken at 600 and 700 microseconds respectively, clearly show the propagation. Schlieren photos taken for flow over the flat plate mounted upside down revealed that choking effect was due mainly to the contour of the under surface of the flat plate in the region where screws attached the leading-edge portion of the plate to the main plate body. Additional contouring of the model was not possible since serious structural weakening of this region would have resulted. This limited the available testing time to approximately 850 microseconds.

Experimental Interaction Heat Transfer

Similarity

The previously discussed experimental and theoretical work indicated that the nature of the adiabatic pure-laminar interaction depends on the Mach and Reynolds numbers and the pressure coefficient associated with the pressure rise across the incident-reflected shock system. Specifically, Equation 1 shows that the dimensionless parameter $(x_i-x_o)/x_o$ describing the upstream extent of the interaction depends only on M_2, Re_o, and C_{p4}. Similarily, the experimental study of Barry et al. (6) indicates that at a fixed Mach number, $(x_i-x_o)/x_i$ is a function only of the Reynolds number and the incident shock strength. The form of Equation 12 also indicates that the ratios of the lengths describing the extent of the interaction depends on the Mach and Reynolds numbers and the

incident shock strength. Thus it was concluded that for the pure-laminar adiabatic interaction occuring on a flat plate, the dimensionless length parameters

$$x_o/x_i,$$

$$(x_r-x_s)/x_i,$$

$$(x_s-x_o)/x_i,$$

are functions only of Mach and Reynolds numbers and incident shock strength. For interactions involving heat transfer the dimensionless length parameters would also depend on the surface to free-stream temperature ratio. Hence the parameters governing the flow pattern in interactions involving heat transfer were assumed to be M_2, Re_i, C_{p4}, and T_w/T_2.

The dimensionless parameter selected to describe the heat-transfer rates in the interaction region was q'/q_{fp}, where q' is the heat-transfer rate at location x from the plate leading edge and q_{fp} is the theoretical heat-transfer rate at x through an undisturbed laminar boundary layer developed from the leading edge of the plate with free-stream conditions and plate surface temperature the same as those present for the interaction under consideration. In addition to the parameters governing the flow pattern, the heat-transfer ratio q'/q_{fp} was assumed to depend on the Prandtl number Pr and the specific heat ratio γ of the gas considered, and on a location parameter taken as x_i/x. Thus, in general,

$$q'/q_{fp} = f(M_2, Re_i, C_{p4}, T_w/T_2, Pr, \gamma, x_i/x)$$

It has been previously noted that for shock-tube testing conditions, T_w/T_2 is a function of M_2. In addition, Pr and γ are essentially constant for gases. Thus the above equation was rewritten as

$$q'/q_{fp} = F(M_2, Re_i, C_{p4}, x_i/x) \qquad \text{Eqn. 31.}$$

Each of the parameters on the right-hand side of Equation 31 is independent of the others.

According to Van Driest (27),

$$\delta/x = f(M_2, Re_2, T_w/T_2)$$

for laminar flat-plate flow. Therefore the use of Reynolds number based on x_i in Equation 31 insures interaction similarity in the sense that the ratio of the flat-plate flow boundary layer thickness at x_i to x_i is the same for all interactions occurring at a fixed Mach and Reynolds number regardless of the magnitude of x_i.

Equation 31 suggested the technique by which heat-transfer rates in the region of interaction were measured using heat-transfer gages located at a fixed distance from the flat-plate leading edge (x_g in Figure 10). At a fixed Mach number and C_{p4}, q'/q_{fp} at $x = x_g$ is a function of Re_i and x_i/x_g. Since Re_i is proportional to P_1 and x_i for a fixed T_1 (see Equation 27), x_i could be varied while Re_i was held

constant through a compensating pressure change. Therefore x_i was taken as the variable in the ratio x_i/x. It was then possible to measure local heat-transfer rates upstream and downstream of the shock-impingement point within a limited range under similar interaction conditions using heat-transfer gages at a single x location on the flat plate.

Variable x_i required that the shock generating wedge and the flat plate be movable relative to each other. This was accomplished by designing the flat plate mounting bracket so that the flat plate could be moved in a direction parallel to the longnitudinal axis of the shock tube.

Figure 15 shows the Re_i x_i/x plane. The range of Re_i available at any x_i/x is that between the two pressure lines which are the limits of initial channel pressure P_1 for which acceptable agreement between experimental flat-plate heat-transfer results and theory was obtained. Indicated for each value of θ are the points in the Re_i x_i/x plane for which heat-transfer results for the interaction case are presented. For convenience the data was taken at fixed values of x_i/x at the various Reynolds numbers indicated. The value of x_i was determined from measurements made on Schlieren photographs. x_i was adjusted by moving the flat-plate model to obtain the values of x_i/x shown in Figure 15. Figure 26, Appendix A, shows the theoretical variation in x_i that would occur for counter times ranging from 490 to 510 microseconds (M_2 = 1.52 $\pm$ 0.02) for θ = 5°. This variation, approximately 0.07

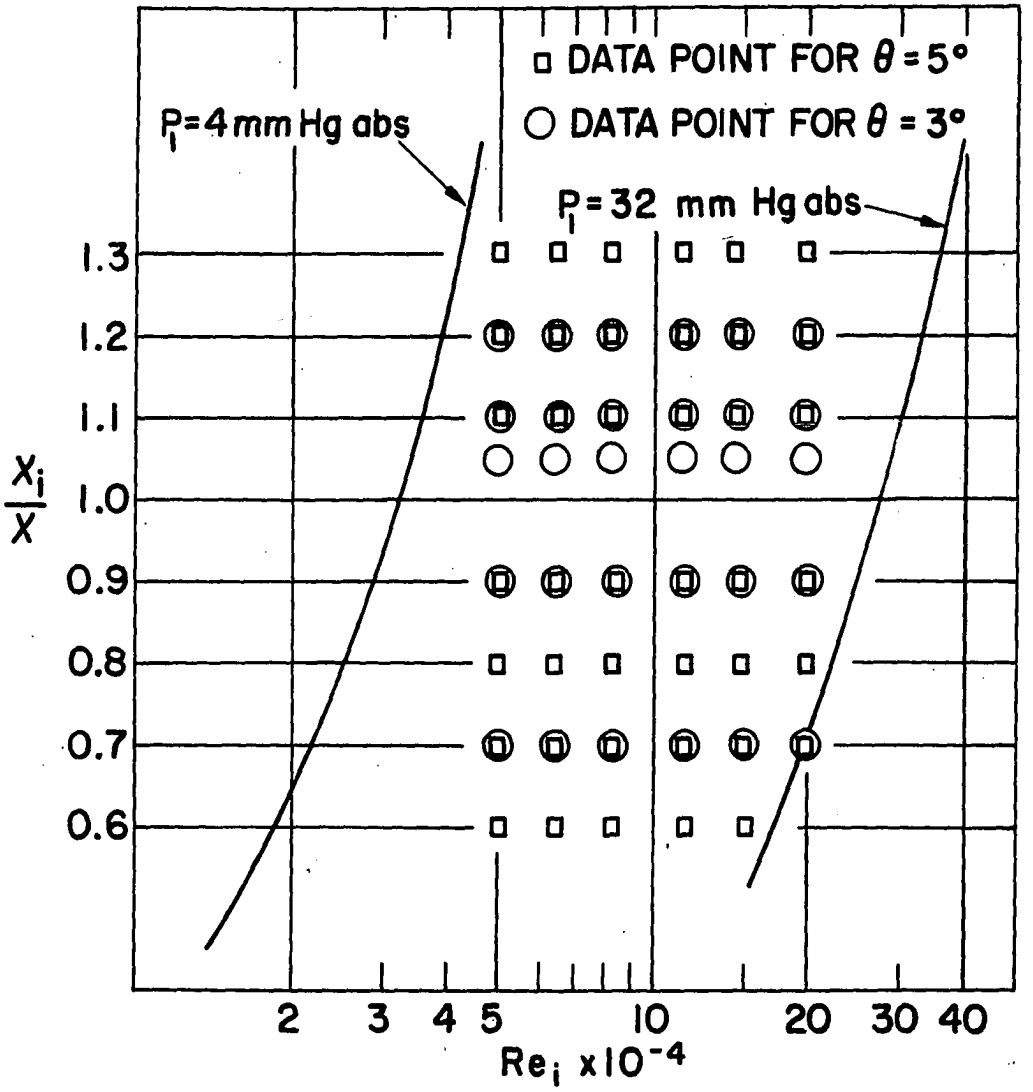

Figure 15. Data points for the shock-wave boundary-layer interaction heat-transfer investigation

inches, was about 30 per cent of the 0.219-inch increment by which x_i was changed to vary x_i/x. Therefore it was felt that the x_i/x grid chosen was as small as could reasonably be used.

Heat transfer measurement

Figures 12A, B, C, D, E, and F are typical Schlieren photos obtained in this investigation for shock-wave boundary-layer interactions. The incident-reflected shock-wave system is clearly visible as is the thickening of the boundary layer in the region of interaction.

Figure 11C shows the output of heat-transfer gages A_2 and B_2 for the interaction case with $\theta = 5°$, $Re_i = 4.95 \times 10^4$ and $x_i/x = 1.2$ (gages upstream of the incident shock wave). The change in slope from positive to negative starting at about 300 microseconds was interpreted to correspond to the passage of the separated region (and the disturbed region just ahead of it) over the gages. Figure 16 shows heat-transfer rates determined by the computer program using data from heat-transfer traces at 20 microsecond intervals for x_i/x values of 1.1, 1.2, and 1.3. The Reynolds number for these curves was 4.95×10^4 and θ was 5°. The decrease in heat-transfer rate below the theoretical flat-plate rates is evident. For $x_i/x = 1.1$ the reduced heat-transfer rate is seen to become reasonably steady after about 350 microseconds while longer times are required to develop reasonably steady rates for the larger values of x_i/x.

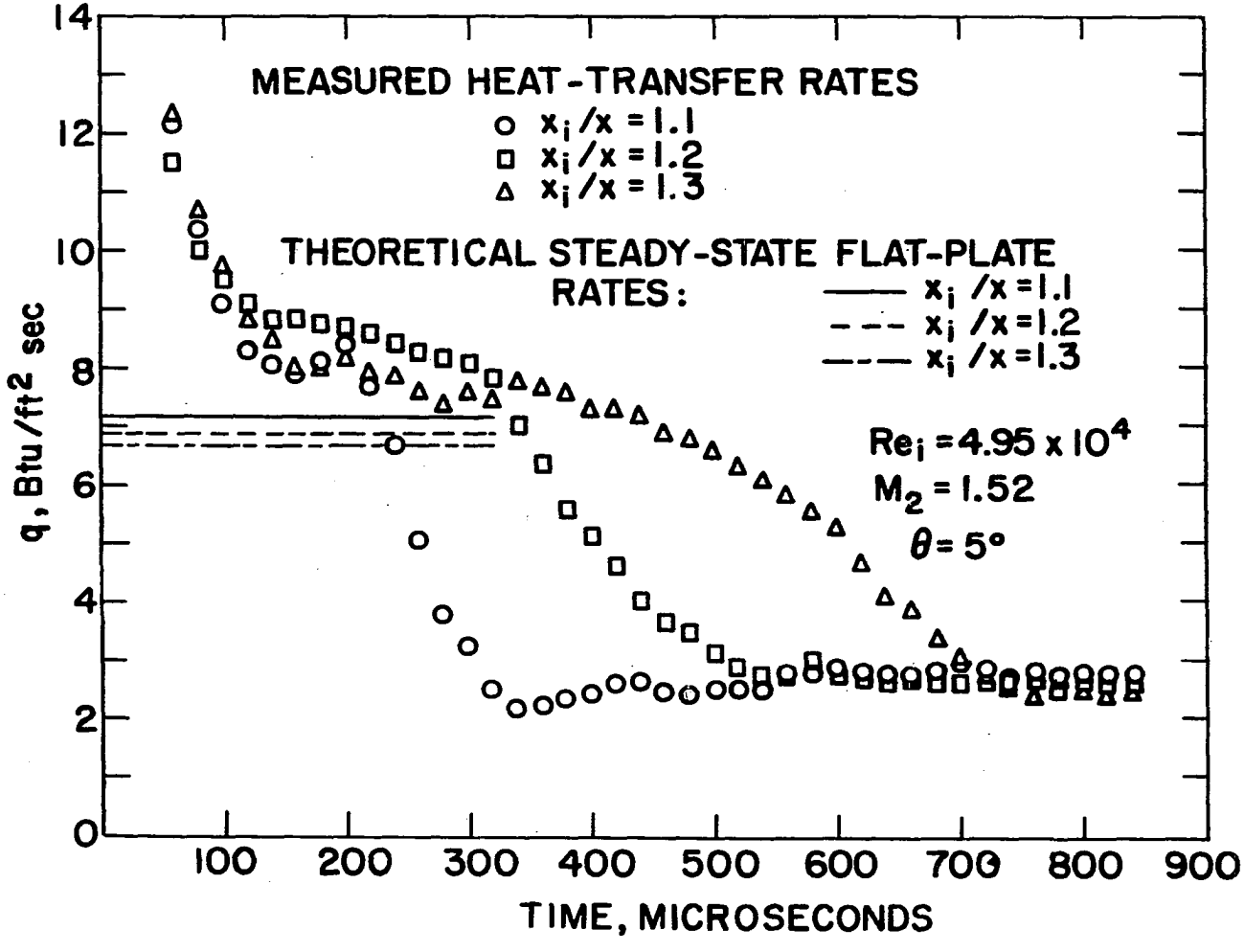

Figure 16. Comparison of heat-transfer curves for the separated region

The heat-transfer results shown in Figure 16 are typical of those for other Reynolds numbers and x_i/x values ranging from 1.05 to 1.3. The characteristic dip appeared in each of the heat-transfer gage output traces, and the heat-transfer rates observed were all less than the corresponding flat-plate rates. Some difficulty was encountered due to the development of nicks in the sharp leading edge of the flat-plate model which were apparently caused by chips of diaphragm material in the flow. Heat-transfer traces recorded when sizeable nicks were present on the leading edge exhibited considerably different characteristics than those observed in Figure 11C. This indicated that the nicks were causing an appreciable disturbance in the flow. When the leading edge was resharpened the shape of the traces returned to that seen in Figure 11C.

In view of the relatively long time required for the separated region to propagate upstream (as indicated by Figure 16) one might question whether fully developed flow was achieved in the testing time available even though the steady heat-transfer rates might suggest that it was achieved. In order to check this Figure 17 was plotted. For each value of θ the time corresponding to the arrival of the separated region as indicated by the dip in the heat-transfer traces was plotted for all data points for $x_i/x>1$ shown in Figure 14. An extrapolation of the results, which is intended only to be qualitative, indicates that the flow development time is of the order of the available testing time (approximately 850

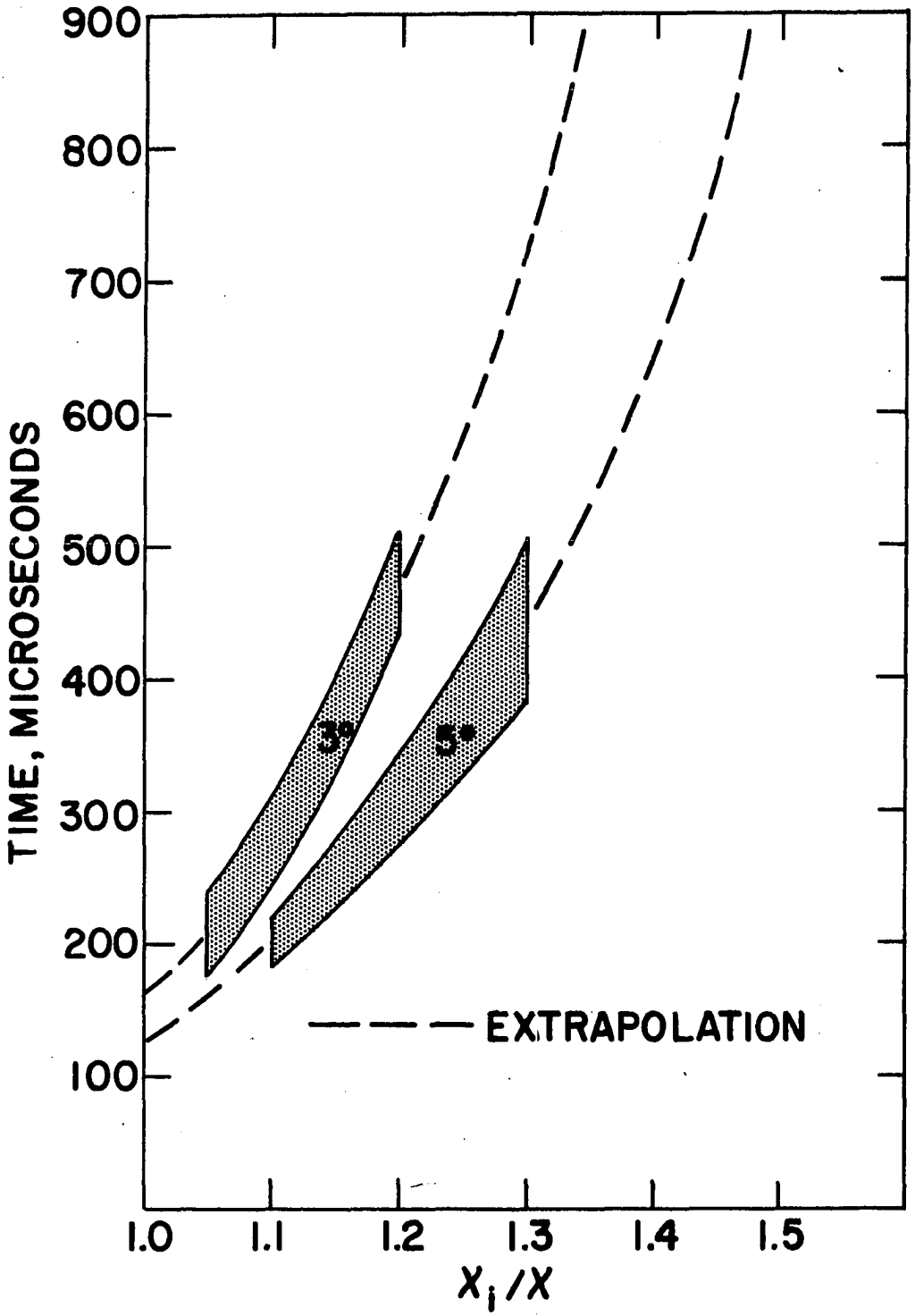

Figure 17. Separated region arrival time for various x_i/x values

microseconds) but longer than the testing time. Although it is reasonable to question the validity of assuming that the heat transfer rates measured under such conditions are those for fully-developed flow, it is felt that there is strong evidence to indicate that the measured heat-transfer rates are those for fully developed flow. Inspection of the typical results in Figure 16 indicates that for $x_i/x = 1.1$, the heat-transfer rate was reasonably steady over the last half of the testing time. Figure 17 suggests a reduction in the velocity of propagation of the separated region with increasing x_i/x, implying that the flow smoothly approaches equilibrium conditions. The absence of any major change in the heat-transfer rate late in the testing time suggests that there would be no major change in the heat transfer rate on complete flow development. In addition, it intuitively seems unreasonable for an intermediate steady state heat-transfer situation to exist. Hence the heat-transfer rates presented for $x_i/x>1$ are those corresponding to the steady-state rates achieved within the testing time available and were considered to be the steady-state rates for fully developed flow. As indicated in Figure 16, larger values of x_i/x exhibited shorter time intervals over which steady heat-transfer rates extended.

It was not possible to obtain steady-state heat-transfer rates at x_i/x values greater than 1.3 for the 5° angle or for x_i/x values greater than 1.2 for the 3° angle since the time required to reach steady state under these conditions was

longer than the available testing time.

Figure 11D presents heat-transfer traces typical of those at high Reynolds numbers for $x_i/x<1$. In general rates observed for $x_i/x<1$ were somewhat more erratic than those observed for flat-plate flow or for $x_i/x>1$. The time required to reach reasonably steady heat-transfer rates was in most cases less than 300 microseconds.

Results are not presented for $x_i/x = 1$ because heat-transfer rates at this location were so erratic that no reasonable steady-state value was reached. These rates varied from less than flat-plate rates to values exceeding flat-plate rates.

RESULTS

Figures 18 to 23 present the results of heat-transfer measurements for the shock wave boundary-layer interactions investigated. q'/q_{fp} is shown as a function of x_i/x for each Reynolds number, Re_i, for which data were taken. Results for both values of θ are shown in each figure. Since there was good agreement between the two gages at each location for flat-plate heat transfer, results are identified in terms of gage location rather than gage number. q_{fp} was evaluated for each case using Eckert's reference enthalpy method. The points shown on the figures are the time-averaged results. The range of the parameter q'/q_{fp} over which the average was determined is indicated for each point by symbols identified on the figures. For x_i/x greater than unity (heat transfer gages upstream of incident shock impingement point) only the upper and lower limits for the group of points at each x_i/x are shown.

In general Figures 18 to 23 indicate that local heat-transfer rates in the separated region (x_i/x greater than unity) are considerably less than those for undisturbed flat-plate flow. For each Re_i and θ, the ratio q'/q_{fp} is seen to be about 0.3 with no apparent trend to indicate a dependence on either Re_i, θ, or x_i/x. Figure 24 is a plot of the results for x_i/x greater than one with no distinction made among results for the various values of x_i/x. This figure indicates

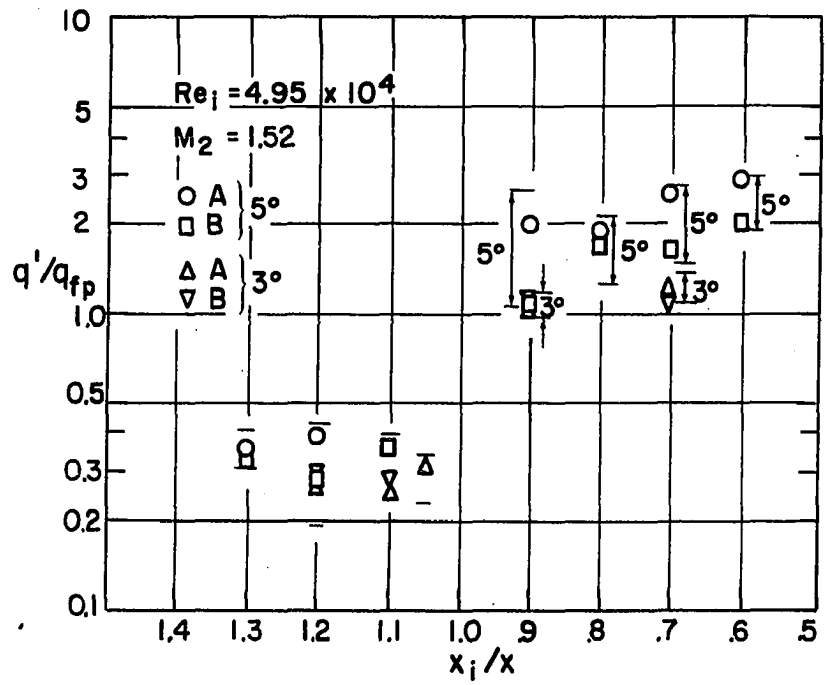

Figure 18. q'/q_{fp} as a function of x_i/x for $Re_i = 4.95 \times 10^4$

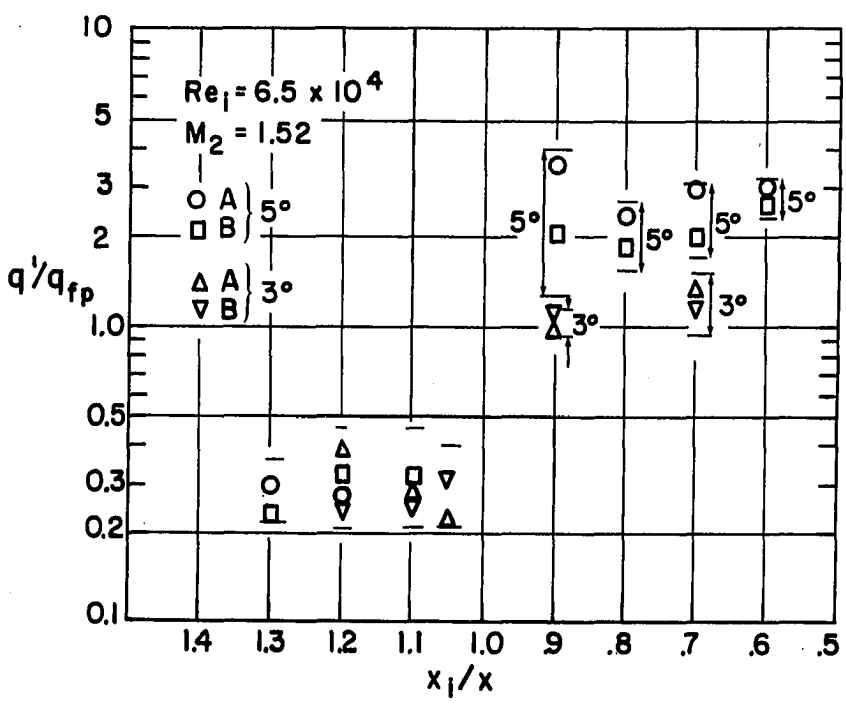

Figure 19. q'/q_{fp} as a function of x_i/x for $Re_i = 6.50 \times 10^4$

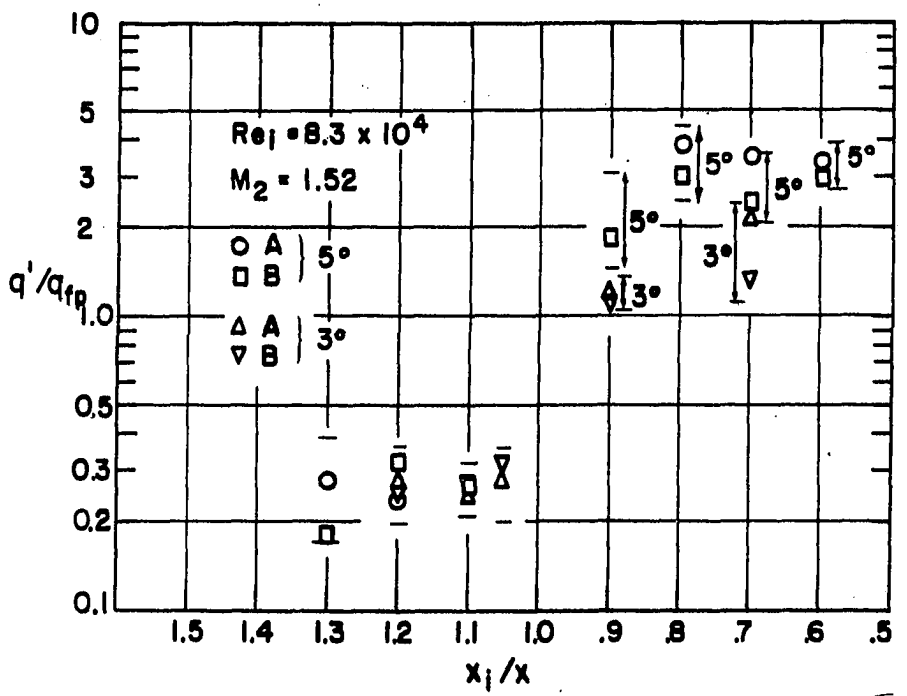

Figure 20. q'/q_{fp} as a function of x_i/x for Re_i = 8.30 x 10^4

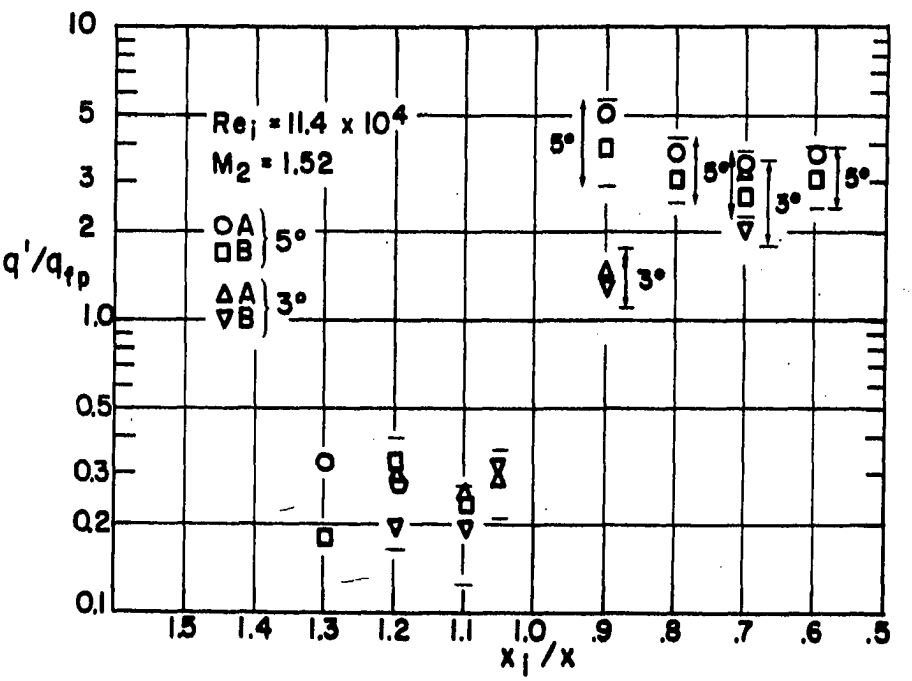

Figure 21. q'/q_{fp} as a function of x_i/x for Re_i = 11.4 x 10^4

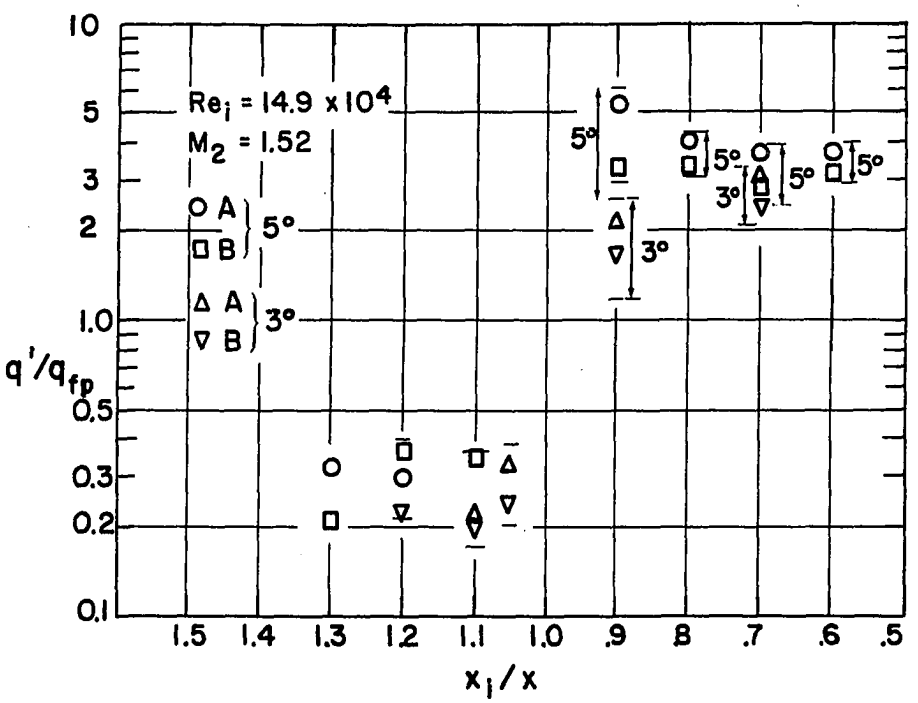

Figure 22. q'/q_{fp} as a function of x_i/x for $Re_i = 14.9 \times 10^4$

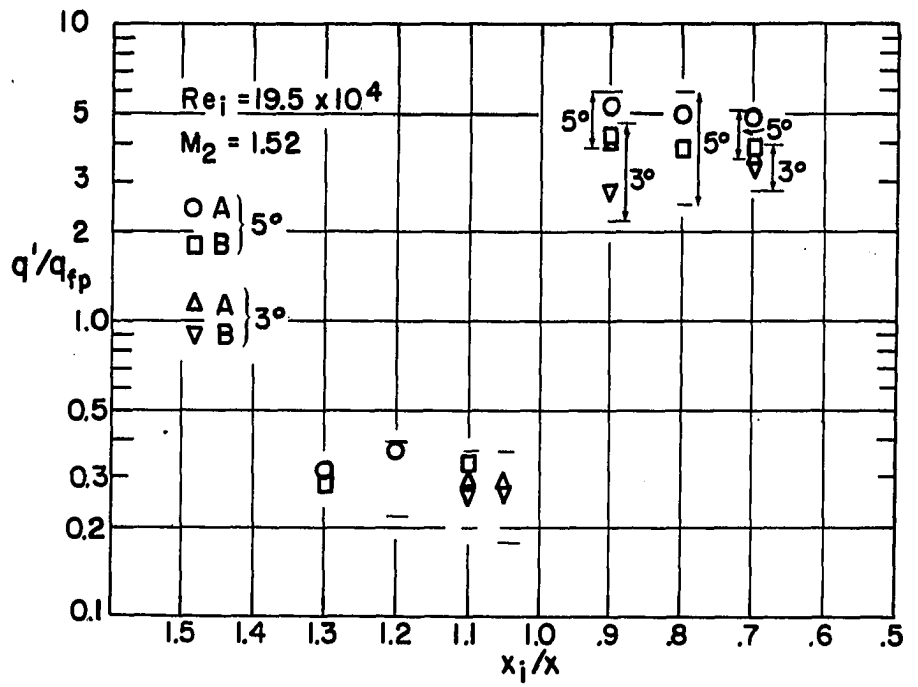

Figure 23. q'/q_{fp} as a function of x_i/x for $Re_i = 19.5 \times 10^4$

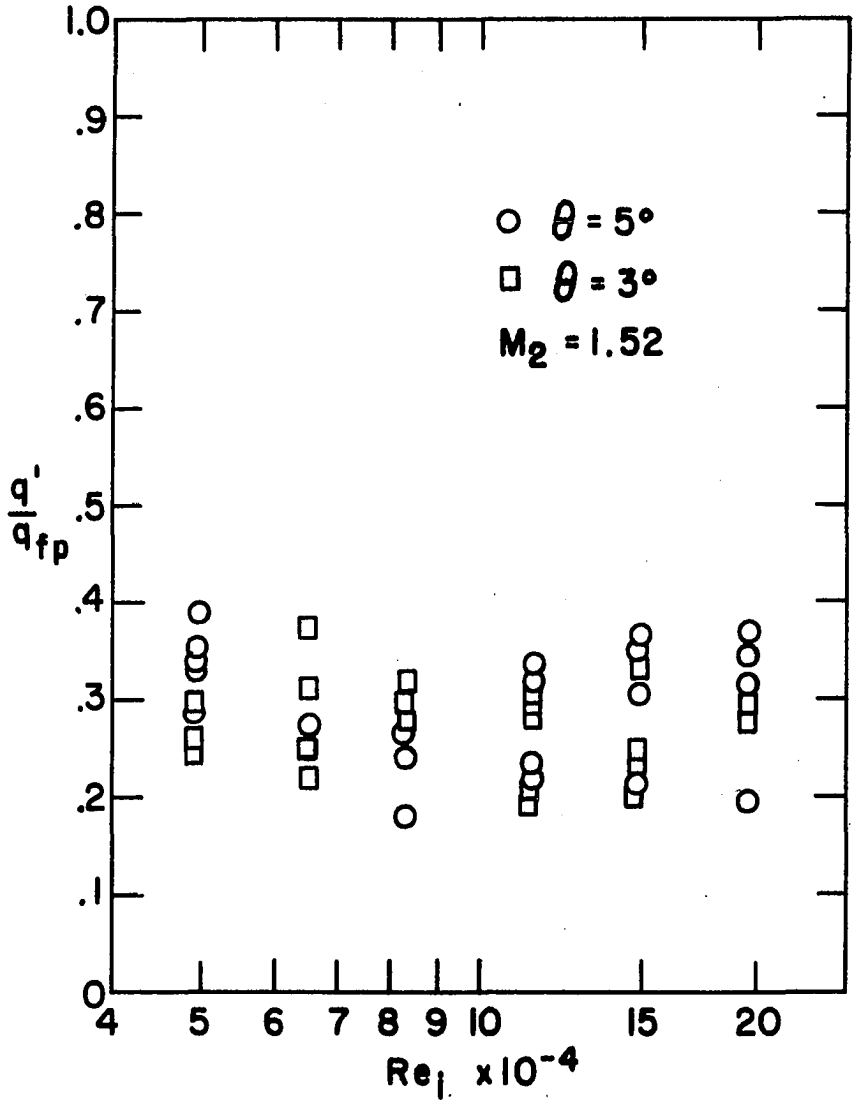

Figure 24. Comparison of heat-transfer results for the separated region

that within the experimental scatter, q'/q_{fp} is independent of Re_i, θ, and x_i/x. For the range investigated, $q'/q_{fp} = 0.3 \pm 0.1$.

The ratio $(x_r - x_s)/x_i$ could not be determined for the interaction studied in this investigation due to the previously-discussed limitation on shock-tube testing time. Since, in addition, q'/q_{fp} could not be determined for the whole separated region, the ratio $\bar{q}_s'/\bar{q}_{fps}$ in the separated region could not be determined for comparison with the results for this ratio determined in other theoretical and experimental studies. However, comparison of results with other experimental studies reviewed shows that the local values of q'/q_{fp} measured in this investigation for the separated region are considerably lower than any local q/q_{fp} values in the other studies of heat-transfer rates in separated regions.

Inspection of the results for x_i/x less than one (gages downstream of the shock impingement point) shows a dependence on both Reynolds number and incident shock strength. This trend is apparent even though measured heat-transfer rates were quite erratic in this region as indicated by the range for each point in the figures. Consider first the results for the 3° angle. It is observed that for the lowest Reynolds number (Figure 18), q'/q_{fp} is near one. For increasing Re_i there is a trend to higher values of q'/q_{fp} for each x_i/x for which results are shown. At $x_i/x = 0.9$, q'/q_{fp} is less than that for $x_i/x = 0.7$ for all Re_i except the largest value,

19.5×10^4, for which q'/q_{fp} is nearly the same for both x_i/x values. Results corresponding to the 5° angle on the whole show a trend similar to that of the results for the 3° angle. For $Re_i = 4.95 \times 10^4$ (Figure 18), smaller values of x_i/x exhibit generally higher q'/q_{fp} values. For Re_i values of 6.5×10^4 and 8.3×10^4, q'/q_{fp} is roughly the same for all x_i/x. For the remaining Reynolds numbers there is, for each Re_i, a trend to lower q'/q_{fp} values with decreasing x_i/x. The behavior of the results for $x_i/x<1$ for both values of θ is quite similar to the previously-discussed behavior of the experimental results obtained by Rom and Seginer (16) for reattaching separated flows.

The fact that for x_i/x less than one gage B gave results consistently lower than gage A is apparent. The absence of this behavior in the heat-transfer results for flat-plate flow indicated a non-uniformity in the interaction. This was probably caused by misalignment of the shock-generator wedge and the flat plate.

The possibility that the increased heat-transfer rates observed for $x_i/x<1$ were due to boundary-layer transition should be considered. Consider again the interactions for $\theta = 3°$. Figures 12B and 12C are typical Schlieren photographs of interactions for this angle. Figure 12B was taken for $Re_i = 11.4 \times 10^4$ at 600 microseconds after region 2 flow arrival at the model station. Within the resolution of the photograph it appears that the boundary-layer was laminar on

reattachment and remained laminar for the length of the flat-plate visible in the photograph. In Figure 12C which is for $Re_i = 19.5 \times 10^4$ (the highest Re_i for which results are presented) it also appears that the boundary-layer remained laminar throughout the interaction and downstream of the interaction. Other features of the interaction patterns in Figures 12B and 12C appear similar to those for the pure-laminar interaction depicted in Figure 2A. Shock-wave boundary-layer interactions which clearly exhibit transition are visible on the upper surface of the shock-generator wedge in Figures 12B, C, D, E, and F. The shock waves formed in the region between the wedge and the upper wall of the shock tube are due to flow choking in this region.

Figure 7 also gives an indication that the interactions for $\theta = 3°$ were pure laminar. The Reynolds number, Re_o, in this figure is based on x_o in Figure 2A. Since the values of x_o are not known for the interactions studied in this investigation, Figure 7 can only be interpreted qualitatively. In any interaction x_o is necessarily less than x_i. Inspection of pressure measurement for adiabatic shock-wave laminar boundary-layer interactions in references 6 and 9 somewhat similar to those of this investigation indicate that x_o is roughly half of x_i. Therefore, Re_o is approximately half of Re_i. On this basis the range of Re_o was about 2.5×10^4 to 10×10^4. For this range Figure 7 indicates that the pressure coefficient for $\theta = 3°$ is in the region above C_{p_i} and

below 3 C_{pp}, the approximate pure-laminar region. Thus there are indications from both the Schlieren photos and Figure 7 that the interactions for $\theta = 3°$ were pure-laminar.

On the basis that Re_o is half Re_i, Figure 7 predicts that the interactions for $\theta = 5°$ were transitional. However, within the resolution of the typical Schlieren photos for $\theta = 5°$ shown in Figures 12D, E, and F, it appears that transition did not occur before or on reattachment of the boundary-layer. In fact, the interaction patterns in these figures are quite similar to that of Figure 2A. The expansion and compression fans downstream of shock impingement are best seen in Figure 12E which was taken for $Re_i = 14.9 \times 10^4$. In addition it appears that the boundary-layer remains laminar downstream of the interaction region. Since all indications point to the fact that the 3° interactions were pure-laminar and that the boundary-layer remained laminar downstream, the similar behavior of the results for each angle at different Reynolds numbers might also suggest that the 5° interactions involved no transition. A particular illustration of similar results is seen in Figures 18 and 22. The results for $\theta = 5°$ and $Re_i = 4.95 \times 10^4$ in Figure 18 are quantitatively similar to those for $\theta = 3°$ and $Re_i = 14.9 \times 10^4$.

In view of the evidence discussed above it is believed that boundary-layer transition did not occur in the interactions studied in this investigation and that the increased heat-transfer rates downstream of the incident shock wave

impingement point were due to heat transfer through laminar boundary-layers.

Determination of q' as a function of x from the results in Figures 18 to 23 can be accomplished through Equation 31 which is repeated here for convenience.

$$q'/q_{fp} = F(M_2, Re_i, x_i/x, C_{p4}) \qquad \text{Eqn. 31.}$$

For a fixed Re_i, C_{p4}, and T_2,

$$q' = [F(x_i/x)]q_{fp}, \qquad \text{Eqn. 32.}$$

since M_2 was fixed in this investigation. If, in addition, x_i is fixed, q' becomes a function of x only and can be determined for a range of x limited by the range of x_i/x. A typical q' versus x curve is shown in Figure 25. This figure is based on the q'/q_{fp} values for 3° and 5° results at $Re_i = 11.4 \times 10^4$ (Figure 21). An x_i of 2.19 inches was arbitrarily chosen, and T_2 was taken as 1790 °R. The points shown in Figure 25 were determined using an average of the average q'/q_{fp} values indicated by gages A and B. Although the predicted results extend over only a short range of x, it appears from Figure 25 that an overall increase in heat transfer would occur as a result of the shock wave boundary-layer interactions occurring at both values of θ.

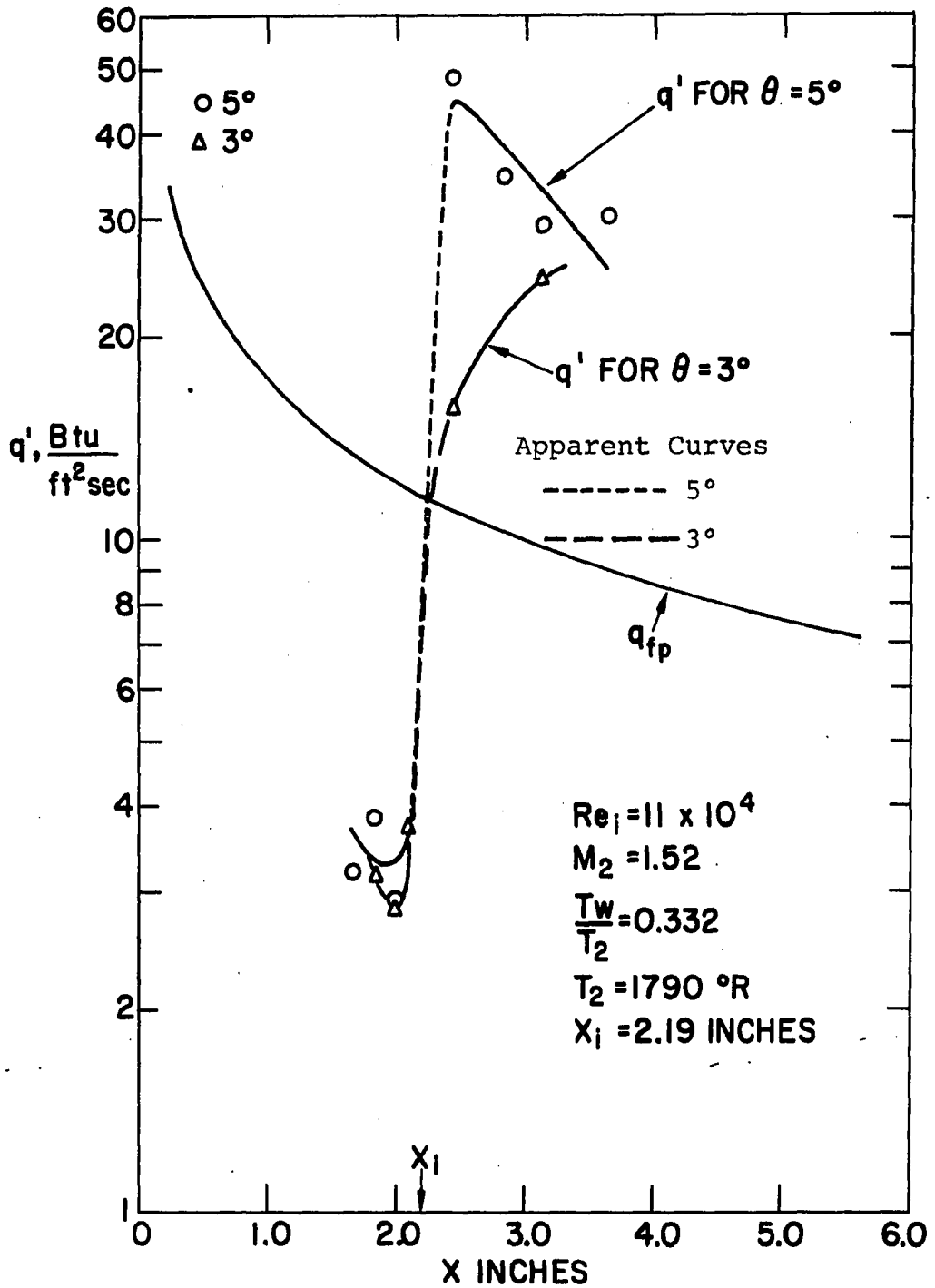

Figure 25. Predicted heat-transfer rates for a shock-wave boundary-layer interaction occurring on a flat plate

CONCLUDING REMARKS

Local heat-transfer rates measured within a limited range in the region of interaction displayed the trends predicted from earlier studies of heat-transfer rates in flows similar to those existing in shock-wave boundary-layer interactions. Even though fully-developed flow was not attained in the interaction region, it is felt that the heat-transfer results presented are those that would exist in fully-developed flow.

Although the heat-transfer rate measurements of this investigation extended over only a limited range of the interaction region and were conducted for a limited range of the controlling parameters, the results should prove useful in the understanding of heat-transfer phenomena in interactions occurring in practice. In addition, the results should be of assistance in developing or verifying theory for the prediction of heat-transfer rates in the interaction region.

RECOMMENDATIONS FOR FURTHER STUDY

Any continuation of the present study using the Iowa State University shock tube should be preceded by an effort to obtain a testing time longer than the flow development time since heat-transfer rates could then be determined throughout the full extent of the separated region.

For the shock-tube flow conditions of this investigation, an increase in testing time could be obtained by eliminating or minimizing the flow choking that occurs above the shock-generating wedge and below the flat-plate model. It appears that this could be achieved by using models which present a smaller frontal area to the flow and by eliminating the present model mounting brackets.

Another approach to solving the testing-time problem would be to study interactions having a shorter flow-development time. In view of the similarity of pure-laminar interactions it appears that a reduction in flow-development time at fixed flow parameters could be achieved by reducing x_i. This would reduce the extent of the interaction and should therefore reduce the flow-development time. A modification of the present flat-plate model would be required to permit heat-transfer gages to be located nearer the leading edge of the plate. An improvement in the data taking technique would result if heat-transfer gages at two or more x locations on the flat-plate model were used.

On attainment of testing time greater than flow-development time, a useful extension of the present study would be the measurement of heat-transfer rates over the entire range of interaction. Numerous other possibilities exist for additional study. The apparent independence of q'/q_{fp} and incident shock strength bears further investigation. Heat-transfer rates for a larger range of Reynolds should be studied with emphasis on the effect of Reynolds number on heat-transfer rates well downstream of the incident shock wave. Extension of the study to other Mach numbers is desirable in order to observe any effect of Mach number on interaction heat-transfer rates. In addition, a continued effort should be made to determine the reason for the disagreement of flat-plate heat-transfer rates with theory for initial channel pressures less than 4 mm Hg abs.

BIBLIOGRAPHY

1. Ferri, Antonio. Experimental results with air foils tested in the high-speed tunnel at Guidonia. U. S. National Advisory Committee for Aeronautics Technical Memorandum 946. 1940.

2. Fage, A. and Sargent, R. F. Shock-wave boundary-layer phenomena near a flat surface. Proceedings of the Royal Society, Series A, 190, No. 1020: 1-20. 1947.

3. Ackert, J., Feldman, F. and Rott, N. Investigation of compression shocks and boundary layers in gases moving at high speed. U. S. National Advisory Committee for Aeronautics Technical Note 1113. 1947.

4. Liepmann, H. W. The interaction between boundary layers and shock waves in transonic flow. Journal of the Aeronautical Sciences 13: 623-637. 1946.

5. _____, Roshko, A. and Dhawan, S. On reflection of shock waves from boundary layers. U. S. National Advisory Committee for Aeronautics Technical Note 2334. 1951.

6. Barry, F. W., Shapiro, A. H. and Neumann, E. P. The interaction of shock waves with boundary layers on a flat surface. Journal of the Aeronautical Sciences 18: 229-238. 1951.

7. Gadd, G. E., Holder, D. W. and Regan, J. D. An experimental investigation of the interaction between shock waves and boundary layers. Proceedings of the Royal Society of London, Series A, 226, No. 1165: 227-253. 1954.

8. Chapman, D. R., Kuehn, D. M. and Larson, H. K. Investigation of separated flows in supersonic and subsonic streams with emphasis on the effect of transition. U. S. National Advisory Committee for Aeronautics Report 1356. 1958.

9. Hakkinen, R. J., Gerber, I., Trilling, L. and Abarbanel, S. The interaction of an oblique shock wave with a laminar boundary layer. U. S. National Aeronautics and Space Administration Memorandum 2-18-59W. 1959.

10. Bogdanoff, S. and Vas, I. Some experiments on hypersonic separated flows. ARS [American Rocket Society] Journal 32: 1564-1572. 1962.

11. Sayano, S., Bausch, H. P. and Donnelly, R. J. Aerodynamic heating due to shock impingement on a flat plate. Douglas Aircraft Company, Inc., Missile and Space Systems Division Report No. SM-41331. 1962.

12. Larson, H. K. Heat transfer in separated flows. Journal of the Aero/Space Sciences 26: 731-738. 1959.

13. Jack, J. R., Wisniewski, R. J. and Diaconis, N. S. Effects of extreme cooling on boundary layer transition. U. S. National Advisory Committee for Aeronautics Technical Note 4094. 1957.

14. Miller, D. S., Hijman, R. and Childs, M. E. Mach 8 to 22 studies of flow separations due to deflected control surfaces. AIAA [American Institute of Aeronautics and Astronautics] Journal 2: 312-321. 1964.

15. Hall, Jerry L. Shock tube investigation of heat transfer in two-dimensional laminar separated flow behind a backward-facing step. Unpublished M.S. thesis. Ames, Iowa, Library, Iowa State University of Science and Technology. 1963.

16. Rom, J. and Seginer, A. Laminar heat transfer to a two dimensional backward facing step from the high-enthalpy supersonic flow in a shock tube. AIAA [American Institute of Aeronautics and Astronautics] Journal 2: 251-255. 1964.

17. Bray, K. N. C., Gadd, G. E. and Woodger, M. Some calculations by the Crocco-Lees and other methods of interactions between shock waves and laminar boundary layers, including effects of heat transfer and suction. Great Britain Aeronautical Research Council Current Paper 556. 1959.

18. Gadd, G. E. A review of theoretical work relevant to the problem of heat transfer effects on laminar separation. Great Britain Aeronautical Research Council Current Paper 331. 1957.

19. Bray, K. N. C. The effect of heat transfer on interactions involving laminar boundary layers. Great Britain Aeronautical Research Council Current Paper 339. 1957.

20. Gadd, G. E. and Attridge, J. L. A note on the effects of heat transfer on separation of a laminar boundary layer. Great Britain Aeronautical Research Council Current Paper 569. 1961.

21. Crocco, L. and Lees, L. A mixing theory for the interaction between dissipative flows and nearly isentropic streams. Journal of the Aero/Space Sciences 19: 649-675. 1952.

22. Knudsen, J. and Katz, D. Fluid dynamics and heat transfer. New York, N. Y., McGraw-Hill Book Company, Inc. 1958.

23. Lees, L. and Reeves, B. L. Supersonic separated and reattaching laminar flows. I. General theory and application to adiabatic boundary layer-shock wave interactions. AIAA Preprint No. 64-4. 1964.

24. Chapman, D. R. A theoretical analysis of heat transfer in regions of separated flow. U. S. National Advisory Committee for Aeronautics Technical Note 3792. 1956.

25. Chung, P. M. and Viegas, J. R. Heat transfer in the reattachment zone of separated laminar boundary layers. U. S. National Aeronautics and Space Administration Technical Note D-1072. 1961.

26. Erdos, J. and Pallone, A. Shock-boundary layer interactions and flow separation. Heat Transfer and Fluid Mechanics Institute Proceedings 1962: 239-254. 1962.

27. Van Driest, E. R. Investigation of laminar boundary layer in compressible fluids using the Crocco method. U. S. National Advisory Committee for Aeronautics Technical Note 2597. 1952.

28. Truitt, R. W. Fundamentals of aerodynamic heating. New York, N. Y., Ronald Press Co. 1960.

29. Jakob, Max. Heat transfer. Volume 2. New York, N. Y. John Wiley and Sons. 1949.

30. Eckert, E. R. G. Engineering relations for heat transfer and friction in high-velocity laminar and turbulent boundary-layer flow over surfaces with constant pressure and temperature. In Hartnett, J. P., ed. Recent advances in heat and mass transfer. pp. 55-81. New York, N. Y., McGraw-Hill Book Company, Inc. 1961.

31. Glass, I. I. and Patterson, G. N. A theoretical and experimental study of shock-tube flows. Journal of the Aerospace Sciences 22: 73-100. 1955.

32. Glass, I. I. and Hall, J. G. Shock tubes. Handbook of supersonic aerodynamics. Volume 6, Section 13. U. S. Bureau of Naval Weapons, NAVORD Report 1488. 1959.

33. Keenan, J. H. and Kaye, J. Gas tables. New York, N. Y., John Wiley and Sons, Inc. 1945.

34. Taylor, B. W. Development of a thin film heat-transfer gauge for shock-tube flows. University of Toronto, Canada, Institute of Aerophysics Technical Note 27. 1959.

35. Vidal, R. Model instrumentation techniques for heat transfer and force measurements in a hypersonic shock tunnel. Cornell Aeronautical Laboratory [Cornell University, Buffalo, N. Y.] Report AD-917-A-1. 1956.

36. Henshall, B. D. and Schultz, D. L. Some notes on the use of resistance thermometers for the measurement of heat-transfer rates in shock tubes. Great Britain Aeronautical Research Council Current Paper 408. 1959.

37. Rabinowicz, J. Measurements of turbulent heat transfer rates on the aft portion of blunt base of a hemisphere cylinder in the shock tube. Jet Propulsion 28: 615-620. 1958.

38. Bromberg, Robert. Use of the shock tube wall boundary layer in heat transfer studies. Jet Propulsion 26: 737-740. 1956.

39. Skinner, G. T. A new method of calibrating thin film gauge backing materials. Cornell Aeronautical Laboratory [Cornell University, Buffalo, N. Y.] Report No. CAL 105. 1962.

40. Keenan, J. H. and Keyes, F. G. Thermodynamic properties of steam. New York, N. Y., John Wiley and Sons, Inc. 1959.

41. Kline, S. J. and McClintock, F. Describing uncertainties in single sample experiments. Mechanical Engineering 75: 3-8. 1953.

ACKNOWLEDGMENTS

The author wishes to express his thanks to Dr. G. K. Serovy who directed the author's thesis work and who served as chairman of the author's graduate study committee; and to Dr. Glen Murphy who served as co-chairman.

The able assistance rendered by Mr. E. J. Felderman in the operation of the shock tube during the course of this investigation is gratefully acknowledged.

Financial assistance from the President's Permanent Objective Fund and the Engineering Experiment Station for model fabrication and the supplies necessary to carry out this study is acknowledged.

The author also notes with appreciation the understanding patience of his wife and family during the years of his graduate study.

APPENDIX A

Sample Calculations

Free-stream properties

From the definition of M_s,

$$V_s = M_s a_1.$$

At $T_1 = 535°R$, from the Gas Tables (33), $a_1 = 1135$ ft/sec. For $M_s = 3.5$,

$$V_s = 3.5\ (1135) = 3980 \text{ ft/sec}$$

From relative velocity considerations,

$$V_2 = V_{2r} + V_s$$

where V_{2r} is the velocity of the gas in region 2 relative to the normal shock wave.

$$V_{2r} = M_{2r} a_2.$$

From the normal shock tables at $M_s = 3.5$,

$$M_{2r} = 0.45115$$

$$P_2/P_1 = 14.125$$

$$T_2/T_1 = 3.315.$$

Therefore,

$$T_2 = 3.315\ (535) = 1770\ °R$$

and

$$a_2 = 2018 \text{ ft/sec.}$$

Thus,

$$V_2 = -(0.45115)(1018) + 3980 = 3078 \text{ ft/sec.}$$

$$M_2 = V_2/a_2 = 3078/2018 = 1.52.$$

For V_s = 3980 ft/sec, the time required for the normal shock to travel the 2.0 ft. between the shock wave detector thin films (Figure 6) is

$$t = 2.0/3980 = 502 \text{ microseconds}$$

which is the time that the Beckman-Berkeley counter (Figure 6) would register. Figure 26 presents the variation in M_2 and T_2 with counter time for T_1 = 535 °R.

Theoretical laminar flat-plate heat transfer

The reference enthalpy was given as

$$i^* = i_2 + 0.5(i_w - i_2) + 0.22(i_{aw} - i_2). \qquad \text{Eqn. 22.}$$

From Equations 17 and 18,

$$r = (Pr^*)^{1/2} = (i_{aw} - i_2)/(i_2^\circ - i_2),$$

where enthalpies replace temperatures in Equation 17. Rearranging the above equation

$$i_{aw} - i_2 = (Pr^*)^{1/2} (i_2^\circ - i_2) = (Pr^*)^{1/2} (V_2^2/2g_cJ). \qquad \text{Eqn. 33.}$$

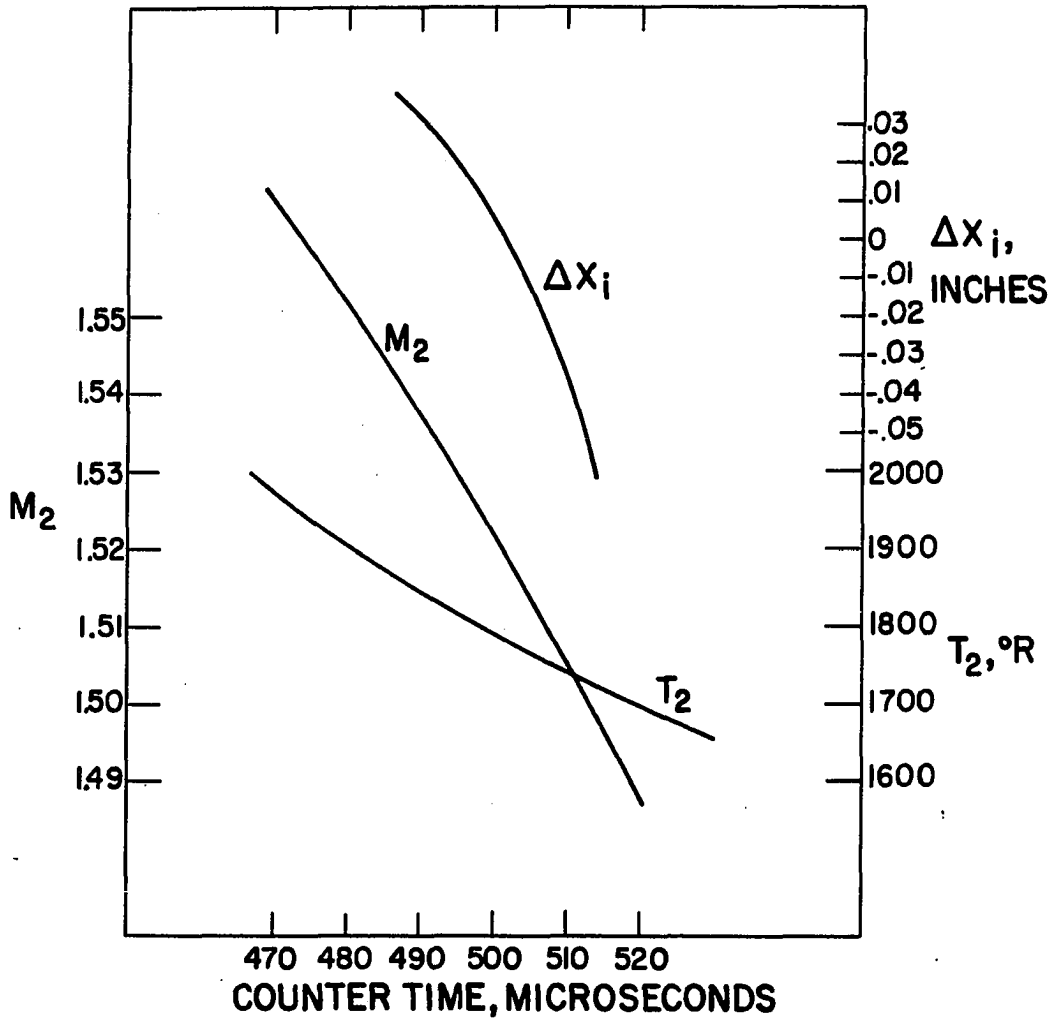

Figure 26. Variation of parameters with counter time (Counter time is the time registered by the Beckman Berkeley counter, Figure 6)

Therefore,

$$i^* = i_2 + 0.5(i_w - i_2) + 0.22(Pr^*)^{1/2} \ (V_2^2/2g_cJ) \qquad \text{Eqn. 34.}$$

From the Gas Tables at 535 °R and 1770 °R respectively,

$$i_w = 127.86 \text{ Btu/lbm.}$$

$$i_2 = 441.55 \text{ Btu/lbm.}$$

Assuming $T^* = 1300$ °R, and $Pr^* = 0.66$, and substituting these values along with $V_2 = 3078$ ft/sec into Equation 34 gives

$$i^* = 318.9 \text{ Btu/lbm.}$$

The corresponding T^* is 1310 °R. Therefore, i^* was taken as the value as listed above, and Pr^* was taken as 0.66.

Equation 21 may be written as

$$(Nu/Pr)^* = 0.332 \ (Re^*)^{1/2} \ (Pr^*)^{-2/3}$$

where the asterisk denotes that the temperature-dependent properties in each of the parameters are evaluated at T^*. For $Pr^* = 0.66$,

$$(Nu/Pr)^* = 0.438 \ (Re^*)^{1/2}$$

which is the relation shown graphically in Figure 14.

Conversion of flat-plate heat-transfer rates to reference coordinates

$$(Nu/Pr)^* = (h_i \ x_g)/\mu^*$$

Substitution from Equation 19 gives

$$(Nu/Pr)^* = q\, x_g/(i_{aw} - i_w)\mu^* \qquad \text{Eqn. 35.}$$

From Equation 33,

$$i_{aw} = i_2 + (Pr^*)^{1/2}\ (V_2^2/2g_cJ). \qquad \text{Eqn. 36.}$$

Substitution of the previously listed values into Equation 36 yielded

$$i_{aw} = 595.5 \text{ Btu/lbm.}$$

From the Gas Tables at $T^* = 1310$ °R, $\mu^* = 231 \times 10^{-7}$ lbm/ft sec. The average heat-transfer rate for the steady-state portion of the heat-transfer rate curve in Figure 13 for gage A_2 was 9.06 Btu/ft^2 sec. Substitution of this value and other listed values along with $x_g = 2.19/12$ ft. into Equation 35 gave

$$(Nu/Pr)^* = 153.5.$$

The corresponding reference Reynolds number was determined as follows:

$$Re^* = V_2\, x_g \rho^*/\mu^* \qquad \text{Eqn. 37.}$$

$$\rho^* = P_2/(RT^*) \qquad \text{Eqn. 38.}$$

$$= (P_2/P_1)(P_1/RT^*)$$

P_1 for the run for which heat transfer results are shown in Figure 13 was 10 mm Hg abs. Thus,

$$\rho^* = (14.125)(10)(2.784)/(53.3)(1310)$$

$$= 0.00564 \text{ lbm/ft}^3$$

where the 2.784 factor in the above substitution is the conversion factor between mm Hg abs and lbf/ft^2. Substitution into Equation 37 gave

$$Re^* = 13{,}700$$

Thus the two coordinates for plotting the data point in Figure 14 are determined.

Determination of q'/q_{fp}

The sample calculations for q'/q_{fp} given below are for the heat-transfer results shown in Figure 16 for $x_i/x = 1.1$, $\theta = 5°$, and $Re_i = 4.95 \times 10^4$. For the portion of the curve beyond 350 microseconds, the average heat-transfer rate was 2.59 $\text{Btu/ft}^2\text{sec}$. From

$$Re_i = (V_2\ x_i\ P_2)/(\mu_2\ R\ T_2) = 4.95 \times 10^4,$$

at

$$V_2 = 3078 \text{ ft/sec}$$

$$T_2 = 1770 \text{ °R}$$

$$\mu_2 = 281 \times 10^{-7} \text{ lbm/ft sec}$$

$$x_i = 1.1(2.19)/12 \text{ ft},$$

the value of P_2 was

$$P_2 = 213 \text{ lbf/ft}^2.$$

Since the following equation applies to flat-plate heat transfer for this investigation,

$$(Nu/Pr)^* = St^*Re^* = 0.438 (Re^*)^{1/2},$$

the reference Stanton number becomes

$$St^* = h_i/(\rho^*V_2) = 0.438 (Re^*)^{-1/2}.$$

From the above equation and Equations 19, 37, and 38,

$$q_{fp} = 0.438\left[\frac{\mu^*V_2 \ P_2}{x_g \ R \ T^*}\right]^{1/2}(i_{aw} - i_w). \qquad \text{Eqn. 39.}$$

Substitution of previously listed numerical values gave

$$q_{fp} = 7.07 \text{ Btu/ft}^2\text{sec}.$$

Therefore,

$$q'/q_{fp} = 2.59/7.07$$

$$= 0.367$$

APPENDIX B

Reduction of Equation 30 for Computer Solution

The following piecewise linear function $\overline{E}(t)$ is determined by reading voltage values from thin-film heat-transfer gage output traces at times

$$t_i = i\Delta t \qquad \text{where } i = 0, 1, 2, \cdots, n.$$

$$\overline{E}(t) = E(t_{i-1}) + \frac{E(t_i) - E(t_{i-1})}{\Delta t}(t - t_{i-1})$$

where

$$t_{i-1} \leq t \leq t_i$$

and

$$i = 1, 2, \cdots, n.$$

The integral in Equation 30 may be written as

$$R(t_n) = \frac{1}{2}\int_0^{t_n} \frac{E(t_n)-\overline{E}(\tau)}{(t_n-\tau)^{3/2}}\,d\tau$$

$$= \frac{1}{2}\sum_{i=1}^{n}\int_{t_{i-1}}^{t_i} \frac{E(t_n)-\overline{E}(\tau)}{(t_n-\tau)^{3/2}}\,d\tau$$

$$= \frac{1}{2} \sum_{i=1}^{n} \int_{t_{i-1}}^{t_i} \left[E(t_n) \right.$$

$$\left. -E(t_{i-1}) - \frac{E(t_i)-E(t_{i-1})}{\Delta t} (\tau - t_{i-1}) \right] \frac{d\tau}{(t_n-\tau)^{3/2}}$$

$$= \frac{1}{2} \sum_{i=1}^{n} \left\{ \left[E(t_n)-E(t_{i-1}) \right] \int_{t_{i-1}}^{t_i} \frac{1}{(t_n-\tau)^{3/2}} d\tau \right.$$

$$\left. - \frac{E(t_i)-E(t_{i-1})}{\Delta t} \int_{t_{i-1}}^{t_i} \frac{\tau - t_{i-1}}{(t_n-\tau)^{3/2}} d\tau \right\} \qquad \text{Eqn. 40.}$$

Considering the first integral in Equation 40,

$$\int_{t_{i-1}}^{t_i} \frac{1}{(t_n-\tau)^{3/2}} d\tau = \frac{2}{\sqrt{t_n-\tau}} \Bigg|_{t_{i-1}}^{t_i} = 2\left[\frac{1}{\sqrt{t_n-t_i}} - \frac{1}{\sqrt{t_n-t_{i-1}}} \right].$$

Eqn. 41.

Considering the last integral in Equation 40, let

$$u = \tau - t_{i-1}$$

$$dv = \frac{d\tau}{(t_n-\tau)^{3/2}} .$$

Thus,

$$du = d\tau$$

$$v = \frac{2}{\sqrt{t_n-\tau}} .$$

Therefore,

$$\int_{t_{i-1}}^{t_i} \frac{(\tau-t_{i-1})}{(t_n-\tau)^{3/2}}\, d\tau$$

$$= \frac{2(\tau-t_{i-1})}{\sqrt{t_n-\tau}} \Bigg|_{t_{i-1}}^{t_i} - 2\int_{t_{i-1}}^{t_i} \frac{d\tau}{\sqrt{t_n-\tau}}$$

$$= \frac{2(t_i-t_{i-1})}{\sqrt{t_n-t_i}} + 4\sqrt{t_n-\tau} \Bigg|_{t_{i-1}}^{t_i}$$

$$= \frac{2\Delta t}{\sqrt{t_n-t_i}} + 4\left[\sqrt{t_n-t_i} - \sqrt{t_n-t_{i-1}}\right] \qquad \text{Eqn. 42.}$$

Substituting Equations 41 and 42 into Equation 40:

$$R(t_n) = \frac{1}{2} \sum_{i=1}^{n} \left\{ 2[E(t_n)-E(t_{i-1})] \left[\frac{1}{\sqrt{t_n-t_i}} - \frac{1}{\sqrt{t_n-t_{i-1}}} \right] \right.$$

$$\left. - \frac{E(t_i)-E(t_{i-1})}{\Delta t} \left[\frac{2\Delta t}{\sqrt{t_n-t_i}} + 4(\sqrt{t_n-t_i} - \sqrt{t_n-t_{i-1}}) \right] \right\}$$

Eqn. 43.

Here it is noted that

$$\sqrt{t_n-t_i} - \sqrt{t_n-t_{i-1}} = \frac{(t_i-t_{i-1})}{\sqrt{t_n-t_i} + \sqrt{t_n-t_{i-1}}} = \frac{-\Delta t}{\sqrt{t_n-t_i} + \sqrt{t_n-t_{i-1}}}.$$

Substituting into Equation 43 and grouping terms,

$$R(t_n) = \sum_{i=1}^{n} \frac{E(t_n)-E(t_i)}{\sqrt{t_n-t_i}} - \sum_{i=1}^{n} \frac{E(t_n)-E(t_{i-1})}{\sqrt{t_n-t_{i-1}}}$$

$$+ 2 \sum_{i=1}^{n} \frac{E(t_i)-E(t_{i-1})}{\sqrt{t_n-t_i} + \sqrt{t_n-t_{i-1}}} \qquad \text{Eqn. 44.}$$

At i = n, the first term in Equation 44 is indeterminate. However, since E(t) was taken as piecewise linear,

$$\lim_{t \to t_n} \frac{K(t_n-t)}{(t_n-t)^{1/2}} = 0$$

Therefore Equation 43 may be written as

$$R(t_n) = \sum_{i=1}^{n-1} \left\{ \frac{E(t_n)-E(t_i)}{\sqrt{t_n-t_i}} - \frac{E(t_n)-E(t_{i-1})}{\sqrt{t_n-t_{i-1}}} + 2\frac{E(t_i)-E(t_{i-1})}{\sqrt{t_n-t_i}+\sqrt{t_n-t_{i-1}}} \right\}$$

$$+ \frac{[E(t_n)-E(t_{n-1})]}{\sqrt{\Delta t}} \qquad \text{Eqn. 45.}$$

Equation 30 may now be written as

$$q(t_n) = \frac{\Gamma}{\alpha\sqrt{\pi}E_{fo}} \left[\frac{E(t_n)}{\sqrt{t_n}} + \sum_{i=1}^{n-1} \left\{ \frac{E(t_n)-E(t_i)}{\sqrt{t_n-t_i}} - \frac{E(t_n)-E(t_{i-1})}{\sqrt{t_n-t_{i-1}}} \right.\right.$$

$$\left.\left. + 2\frac{E(t_i)-E(t_{i-1})}{\sqrt{t_n-t_i}+\sqrt{t_n-t_{i-1}}} \right\} + \frac{E(t_n)-E(t_{n-1})}{\sqrt{\Delta t}} \right] \qquad \text{Eqn. 46.}$$

The only approximation involved in the use of Equation 46 is the piecewise linear approximation of E(t). Equation 46 was programed for solution on the I.S.U. Cyclone digital computer. Figure 27 is a flow diagram of the program.

Data Reduction

In order to accurately read voltage values from the heat-transfer gage output traces it was necessary to enlarge the traces. This was accomplished by first making a transparent reproduction of the Polaroid photo of the oscilloscope trace.

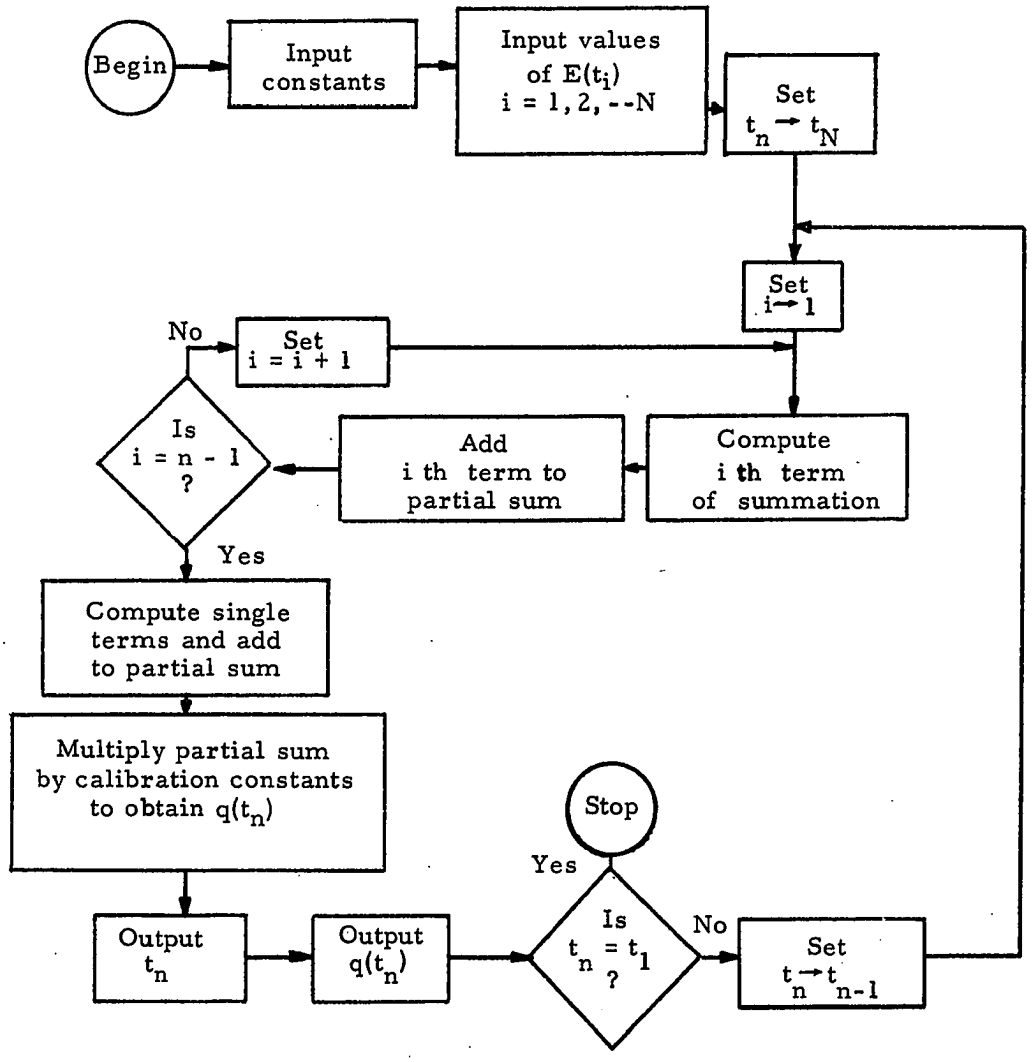

Figure 27. Flow diagram for computer program

This was then used to project the trace onto graph paper, the grid of which was matched to the oscilloscope grid, and the trace was transferred to the graph paper by hand tracing. In this manner an eight-fold enlargement of the trace was obtained and voltage values could be accurately read at 20 microsecond intervals.

The heat-transfer rates in Figure 13 were determined from the traces in Figure 11A. Input voltage values, times, and the resulting heat-transfer rates determined through use of the computer program are shown in Table 2 for Gage A_2. The values of Γ, α, and E_{fo} for Gage A_2 which are also input to the computer solution of Equation 46 are listed in Table 3, Appendix C. The technique described here was used in the reduction of all of the data obtained during the course of this investigation.

Table 2. Computer program input and output for Gage A_2 trace in Figure 11A

Input		Output
Time, Microseconds	Voltage, Millivolts	Heat-transfer Rate, Btu/ft^{2}sec
0	0	-
20	2.86	46.90
40	2.96	21.04
60	3.01	16.40
80	3.05	14.08
100	3.09	12.68
120	3.11	11.40
140	3.14	10.74
160	3.16	10.02
180	3.20	9.82
200	3.24	9.55
220	3.30	9.55
240	3.35	9.43
260	3.41	9.40
280	3.46	9.27
300	3.52	9.27
320	3.59	9.32
340	3.64	9.10
360	3.69	9.00
380	3.75	9.06
400	3.81	9.02
420	3.86	9.06
440	3.93	9.10
460	3.99	9.19
480	4.04	8.90
500	4.08	8.90
520	4.14	8.94
540	4.19	8.87
560	4.24	8.85
580	4.28	8.60
600	4.31	8.56
620	4.36	8.60
640	4.41	8.68
660	4.46	8.71
680	4.51	8.73
700	4.55	8.57
720	4.59	8.53
740	4.63	8.41
760	4.66	8.35
780	4.69	8.23
800	4.71	8.00

APPENDIX C

Gage Calibration

Skinner (39) presents a simple method for determining the quantity $\Gamma = (k\rho c_p)^{1/2}$ which appears in Equations 30 and 46. The method involves application of a repeatable electrical energy input to the thin-film gage. The response of the gage (voltage change across the gage versus time) on application of the electrical pulse is observed under two conditions. First the gage is exposed to air and pulsed, in which case the electrical energy is dissipated into the backing material with a negligible amount being dissipated to the air. Next the gage is immersed in water at the same temperature as the air. In this case the electrical energy is dissipated into both the backing material and the water. The response curves for the two cases are then used to determine Γ by the following relation given by Skinner.

$$\Gamma = \Gamma_w \left(\frac{A_a}{A_w} - 1\right)^{-1}, \qquad \text{Eqn. 47.}$$

where A_a and A_w are the amplitudes of the voltage variation for the gage (taken at a suitable time) for gage exposure to air and water respectively. The voltage variation with time differs only in amplitude for the two cases since a repeatable electrical energy pulse is used. Hence the amplitudes in Equation 47 may be determined at any convenient time.

r_w may be accurately evaluated through the use of reference 40.

The bridge circuit used in the calibration of the thin-film gages used in this investigation is shown in Figure 28. A clean step in voltage input to the bridge was obtained by using a mercury switch. R_1 in Figure 28 was chosen approximately twice the film resistance. Therefore, since only a small change in film resistance occurred after closing the switch, the film current was essentially constant, resulting in a step power input to the gage. It has been shown (15, 36) that a step in power input to a thin-film gage results in a parabolic variation of surface temperature with time. Therefore, considering Equation 29, a parabolic voltage-time response would be expected using the circuit of Figure 28, provided the bridge was initially balanced. Otherwise a parabola superimposed on the initial bridge unbalance would result. In practice it was found that it was not possible to obtain exact bridge balance even though a good quality potentiometer and a gated pulse generator operating at a very low power level were used in an attempt to balance the bridge. Hence direct use of Equation 47 was not possible.

In view of the bridge balancing difficulty another approach was taken. For step-power pulsing the following equations could be written for pulsing in air and water respectively.

$$(\Delta E_f)_a = k_a (t)^{1/2}$$

$$(\Delta E_f)_w = k_w (t)^{1/2}$$

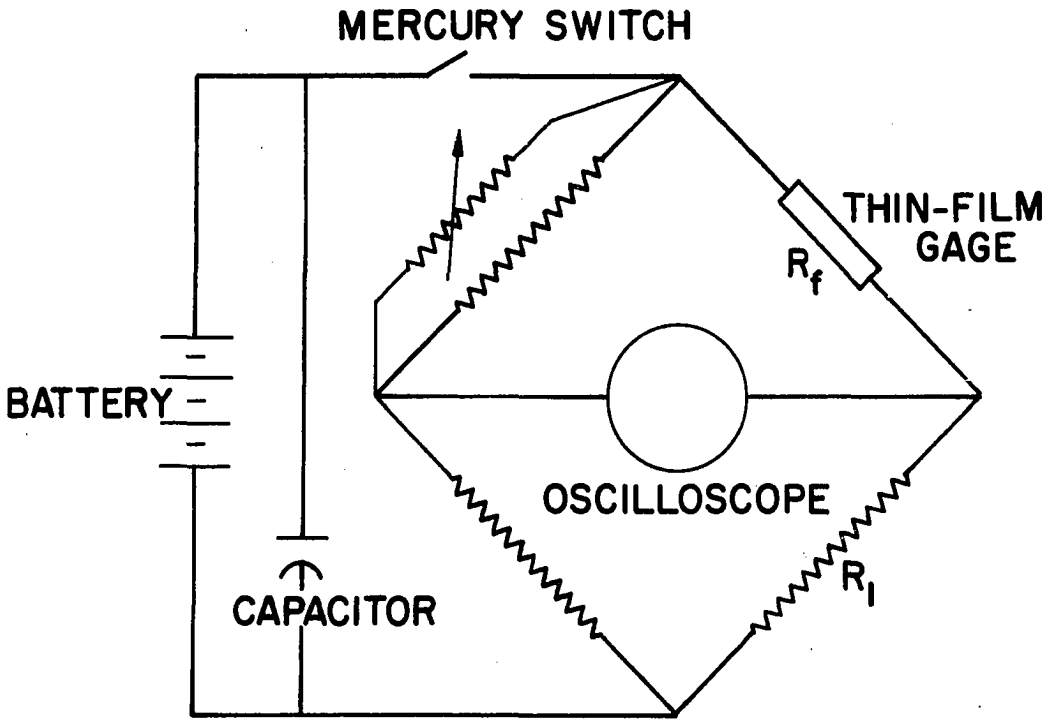

Figure 28. Thin-film heat-transfer gage calibration circuit

Here the time t is measured from the time the voltage is applied and ΔE_f is the film voltage change. k_a and k_w are respectively the slopes of the ΔE_f versus $(t)^{1/2}$ response curves for air and water. From the above equations it is evident that the ratio A_a/A_w in Equation 47 can be replaced by k_a/k_w. The latter ratio can be determined accurately since k_a and k_w are not effected by initial bridge unbalance. The only requirements are that the time zeros be known for the gage calibration response curves and that a step power pulse be used. By triggering the oscilloscope horizontal sweep from the mercury switch the time zero was established.

Figure 29 shows a typical set of curves used in determining Γ. The circled points shown were obtained from enlarged oscilloscope photos of the response curves. The parabolic nature of the response curves is evident in the figure. Thus substitution of k_a/k_w for A_a/A_w in Equation 47 was justified.

The temperature coefficient of resistance α of the thin-film gage which appears in Equations 30 and 46 was determined by plotting film electrical resistance against temperature. Values for this plot were obtained by measuring the resistance of the gage while it was immersed in a constant temperature oil bath. A range of temperature between room temperature and 200 °F was covered.

Table 3 is a summary of important quantities for each thin-film heat transfer gage used in this investigation.

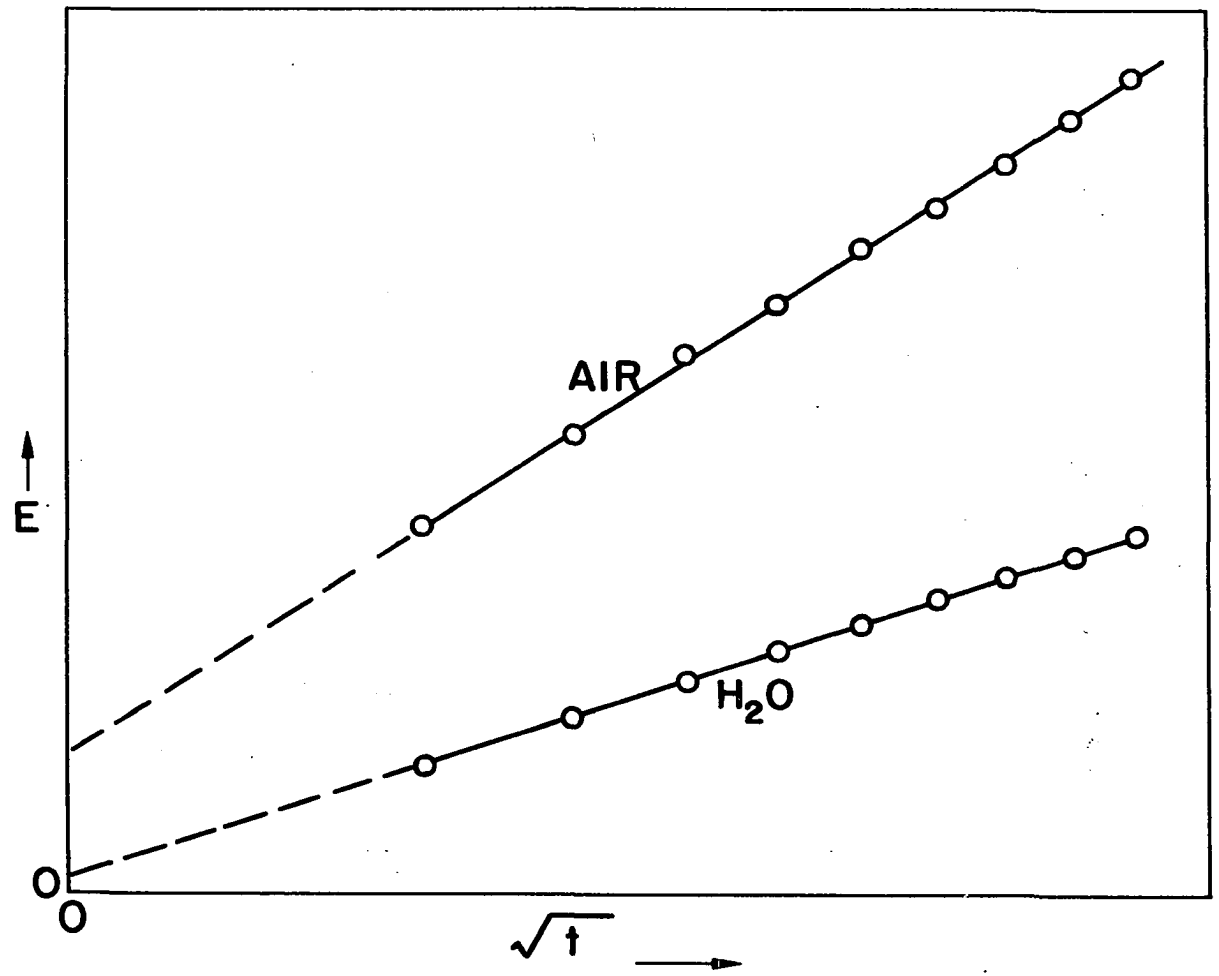

Figure 29. Typical curves used in the determination of Γ

Table 3. Summary of thin-film gage parameters

Gage identification	Gage resistance,* ohms	α^*, $(°R)^{-1}$	Γ $Btu/ft^2\ °R\sqrt{sec}$	E_{fo}, volts
A_1	268.2	0.00124	0.0782	0.80
B_1	191.7	0.00131	0.0696	0.88
A_2	176.7	0.00140	0.0765	0.84
B_2	106.1	0.00138	0.0723	0.69

*At 535 °R.

APPENDIX D

Uncertainty of Heat Transfer Results

The method of Kline and McClintock (41) was used to estimate the uncertainty of the measured heat-transfer rates and of the final results. In single sample experiments where the result R is a function of independent variables v_1, v_2, $\cdots$, v_n, the uncertainty, W_R, of the result R is given by

$$(W_R)^2 = \left(\frac{\partial R}{\partial v_1} W_{v_1}\right)^2 + \left(\frac{\partial R}{\partial v_2} W_{v_2}\right)^2 + \cdots + \left(\frac{\partial R}{\partial v_n} W_{v_n}\right)^2 \quad \text{Eqn. 48.}$$

The uncertainty intervals W_{v_n} are estimated by the experimenter. The odds that a particular observation will fall within the specified range should be indicated. In this investigation the uncertainty intervals were estimated on the basis of 10 to 1 odds.

Designating the quantity within the brackets in Equation 46 as S, Equation 46 may be written as

$$q = \frac{\Gamma}{\alpha\sqrt{\pi}} \frac{S}{E_{fo}} = \frac{\Gamma}{\alpha\sqrt{\pi}} S'$$

where $S' = S/E_{fo}$. S' is taken as the variable in the uncertainty analysis since S and E_{fo} are not independent. (The voltage values used to determine S and the voltage value E_{fo} were measured using the same instrument.)

Application of Equation 48 yields the following expression for the uncertainty in q.

$$(W_q/q)^2 = (W_\Gamma/\Gamma)^2 + (W_{S'}/S')^2 + (-W_\alpha/\alpha)^2 \quad \text{Eqn. 49.}$$

Three sets of curves similar to those in Figure 29 were used in the determination of Γ for each thin-film heat-transfer gage. From these curves it was estimated that W_Γ/Γ was approximately 8 per cent. From the plot of gage resistance versus temperature used to determine α for the gages it was estimated that W_α/α was 3 per cent. A large error in α could result from high contact resistance at the electrical connections to the thin-film gages, but since the connections were made by soldering it was assumed that the contact resistances were negligible. For the flat-plate heat-transfer case, the quantity $W_{S'}/S'$ was estimated to be 5 per cent. This estimate was based on the evaluation of q at fixed Γ and α through use of the computer program for several independent readings of voltage values from a typical flat-plate heat-transfer trace. Substitution of the above-listed uncertainty intervals into Equation 49 gave W_q/q = 9.9 per cent for measured flat-plate heat-transfer rates.

The uncertainty in the ratio q'/q_{fp} was determined as follows. q_{fp} is given in a convenient form by Equation 39. The uncertainty intervals for all terms in this equation except the pressure term were assumed to be small. At a fixed

Mach number in shock tube flow, P_2 is related to P_1 by a constant. Therefore for the uncertainty analysis q_{fp} was proportional to $(P_1)^{1/2}$. Application of Equation 48 gave the uncertainty in q'/q_{fp}.

$$\left[\frac{W_{q'/q_{fp}}}{q'/q_{fp}}\right]^2 = (W_{q'}/q')^2 + [-\tfrac{1}{2}\,(W_{P_1}/P_1)]^2. \quad \text{Eqn. 50.}$$

Experience indicates that $W_{q'}/q'$ is dependent on the shape of the thin-film heat-transfer gage trace. For the separated region ($x_i/x>1$), $W_{S'}/S'$ was estimated to be 10 per cent. W_{P_1}/P_1 was strongly dependent on the pressure level since it was estimated that the uncertainty in pressure measurement was 0.8 mm Hg abs. Therefore, for the lowest value of P_1, 4 mm Hg abs, W_{P_1}/P_1 was 20 per cent; for P_1 = 32 mm Hg abs, W_{P_1}/P_1 = 2.5 per cent. For the case of $x_i/x>1$ and P_1 = 4 mm Hg abs, Equations 49 and 50 gave an uncertainty in q'/q_{fp} of 16.5 per cent, which is the largest uncertainty that would be expected for the results in the separated region.

For $x_i/x<1$, $W_{S'}/S'$ was estimated to be 5 per cent. For P_1 = 4 mm Hg abs and W_{P_1} = 0.8 mm Hg abs, the uncertainty in q'/q_{fp} for the case of $x_i/x<1$ was, by Equations 49 and 50, 14.1 per cent. This is the largest uncertainty expected for the heat transfer results presented for the region downstream of the incident shock wave intersection point.